Crystalline comet dust: Laboratory experiments on a simple silicate system

S. P. THOMPSON,[1] S. FONTI,[2] C. VERRIENTI,[2] A. BLANCO,[2] V. OROFINO,[2] and C. C. TANG[1]

[1]Daresbury Laboratory, Warrington, Cheshire WA4 4AD, UK
[2]Dipartimento di Fisica, Universita di Lecce, C. P. 193 - Via Arnesano, 73100 Lecce, Italy
*Corresponding author. E-mail: s.p.thompson@dl.ac.uk

Abstract–Spectra for certain comets show the presence of crystalline silicate dust grains believed to have been incorporated during comet formation. While grain crystallization is widely assumed to result from the thermal annealing of precursor amorphous grains, the physical processes behind the silicate amorphous-to-crystalline transition are poorly understood. This makes it difficult to place constraints on the evolutionary histories of both grains and comets, and consequently, on the nebular conditions in which they formed. It has, therefore, become necessary to study this process in the laboratory using simulated grain materials. In this paper, we discuss recent results from laboratory investigations into a basic amorphous $MgSiO_3$ silicate annealed in the region of 1000 K. Our object is not to model the behavior of dust grains per se, but to study the underlying process of crystallization and separate the physics of the material from the astrophysics of dust grains. In our experiments, we bring together spectroscopic measurements made in the infrared with the high resolution structural probing capabilities of synchrotron X-ray powder diffraction. The combined use of these complementary techniques provides insights into the crystallization process that would not be easily obtained if each was used in isolation. In particular, we focus on the extent to which the identification of certain spectral features attributed to crystalline phases extends to the physical structure of the grain material itself.

Specifically, we have identified several key features in the way amorphous $MgSiO_3$ behaves when annealed. Rather than crystallize directly to enstatite ($MgSiO_3$) structures, in crystallographic terms, amorphous $MgSiO_3$ can enter a mixed phase of crystalline forsterite (Mg_2SiO_4) and SiO_2-rich amorphous silicate where structural evolution appears to stall. Spectroscopically, the evolution of the 10 μm band does not appear to correlate directly with structural evolution, and therefore, may be a poor indicator of the degree of crystallinity. Indeed, certain features in this band may not be indicators of crystal type. However, the 20 μm band is found to be a good indicator of crystal structure. We suggest that forsterite forms from the ordering of pre-existing regions rich in SiO_4 and that this phase separation is aided by a dehydrogenation processes that results in the evolutionary stall. The implications of this work regarding future observations of comets are discussed.

INTRODUCTION

Over the years, many varied ideas concerning the origin of comets have been proposed. Broadly speaking, these fall between either interstellar or solar system formation. The currently favored model is of comets and planets forming together within a nebular disk encircling an already existing protosun. Within the disk dust, grains are thought to have accumulated first into kilometer-sized cometary bodies and then into larger planetary ones (Bailey 1994). If this was the case, the chemistry and mineralogy of present day observable comets should carry much information about conditions in the early solar nebula as they should represent repositories of the unused leftovers from the solar system building process. In particular, most comets probably formed in the region of the solar nebula between ~5 and ~30 AU from the sun before being gravitationally scattered to the outer edges of the solar system by the large planets. However, models also suggested an additional formation and scattering zone in the Neptune region (Safronov 1972; Fernandez and Ip 1981, 1983; Ip and Fernandez 1988) and, with the discovery of the Edgeworth-Kuiper belt, there came the prospect of extended comet formation over an entire disk possibly stretching as far out as 1000 AU. It is now accepted that Jupiter would have mostly

scattered planetesimals to gravitationally unbound orbits, so the majority of present day Oort cloud comets will have either formed well outside Jupiter's orbit (Hills 1982; Hills and Sandford 1983) or, in certain cases, at the Oort cloud distance itself (Bailey 1987). Table 1 summarizes the relative scattering contributions to the Oort cloud by the large planets along with estimates of the highest mid-plane temperatures of the nebular gas at the planetary orbits. The temperatures shown are those predicted at the time of mid-plane sedimentation and are very low. Edgeworth-Kuiper belt comets are assumed to have formed in situ and would therefore have sampled even more distant (i.e., much cooler) regions of the nebula (out to ~45 AU, Weissman 1995).

Formation of Cometary Silicate Crystals

In view of the above, comets can be regarded as cold-formed objects originating in the cool outer regions of the early solar nebula, constituting assemblages of largely unaltered, pristine presolar interstellar material (Napier and Clube 1997). Given this, the presence in certain comet spectra of sharp infrared (IR) 11.2 μm subfeatures embedded in an otherwise amorphous 10 μm silicate band is difficult to explain as the carrier for this subfeature is now recognized as being crystalline olivine grains (Campins and Ryan 1989; Colangeli et al. 1995, 1996). Crystalline silicates, however, do not constitute a readily observable component of interstellar dust (Lutz et al. 1996; Demyk et al. 1999), which is the assumed precursor of nebular dust, even though the presence of crystalline silicate is well-established in the spectra of certain old evolved oxygen-rich stars (e.g., Asymptotic Giant Branch [AGB stars]) known to be the main source of interstellar dust (Kemper et al. 2001). While Greenberg et al. (1996) argued that comet crystals are actually amorphous silicates annealed in situ in comet comae after many passages at perihelion, an 11.2 μm sub-feature has also been detected in the dynamically young comet Mueller (Hanner et al. 1994a), the orbital characteristics of which suggest it has not made many passages near the sun. This, along with laboratory evidence suggesting the rate of silicate crystallization slows

Table 1. Characteristics of Oort cloud comet forming zones. Mid-plane temperatures refer to the epoch of dust sedimentation into mid-plane orbits in solar nebula disk (after Delsemme 1999).

Comet forming zone	Jupiter	Saturn	Uranus	Neptune
Distance (AU)	5.2	9.54	19.218	30.06
Highest mid-plane temp. (K)	230	140	70	50
% Contribution to Oort cloud				
From Safronov (1972)	8	16	24	52
From Ip and Fernandez (1988)	4	12	34	50

dramatically at lower temperatures (Hallenbeck, Nuth, and Daukantas 1998), points to grain crystallization having occurred prior to the arrival of the comet in the inner solar system. Unfortunately, the probable formation temperatures of comets (Table 1) are far below the ~1000 K temperature required for the crystallization of amorphous silicate. For these reasons, the unique origin of cometary silicate crystals is still contentious, with several possibilities being considered:

• Presolar amorphous interstellar grains annealed in the solar nebula.
• Grains formed as crystals by direct inner-solar nebular condensation.
• Presolar relic stardust grains formed in the atmospheres of evolved oxygen-rich stars, either by annealing amorphous grains or by direct condensation.

Models for the collapse of the early solar nebula (Chick and Cassen 1997) indicate that more than 50% of the grains surviving as far in as 1 to 3 AU would reach temperatures of ~1000 K. If silicate crystals are annealed presolar interstellar amorphous grains, their widespread presence in comets would imply that a significant proportion of all grains present in the outer nebula during comet formation must have been annealed beforehand. Both this and the possibility of grains condensing directly as crystals in the inner regions are likely to require the existence of a transport mechanism to deliver them from the hot inner zones (close to the orbital regions of the terrestrial planets) out to the cooler comet forming zones. The proposed trend (Sitko et al. 2000) for the appearance of silicate spectral features to change from amorphous to crystalline as a function of age for Herbig Ae/Be stars (young stars that have not reached the main sequence) could suggest the action of a continuous mixing process (Nuth 1999), while the proposed steady flow mechanism for material above and below the nebular mid-plane (Prinn 1990; Stevenson 1990) might also be sufficient to deliver processed inner-nebular material to the comet forming zones (Nuth 1999; see also the turbulent mixing mechanism of Bockelée-Morvan et al. 2002).

Despite the lack of detail regarding possible transport mechanisms, if comets do contain primitive materials sampled from various points in the solar nebula, the comet population will likely contain a variety of assemblages of raw interstellar grains, pristine high temperature condensates, plus melted and agglomerated grains originating from the hotter inner reaches of the nebula. Depending on their size and composition, precursor interstellar grains are likely to survive the change from the initial cold presolar molecular cloud to the hotter solar nebula as far in as 1 to 3 AU (Chick and Cassen 1997) and could also either be incorporated into comets intact or first melted and then recondensed. It also seems plausible that comet formation was ongoing throughout most of the solar disk's history, so that earlier comets probably differ in composition from later ones. In the earliest comets, amorphous interstellar grains are likely to dominate, while

later comets should contain more highly processed grains. Crystalline spectral features may, therefore, also be an indicator of comet age (Nuth, Hill, and Kletetschka 2000).

Harker and Desch (2002), however, have proposed an alternate scenario. For certain disk accretion rates, models suggest the solar nebula should have been gravitationally unstable beyond ~5 AU for long periods throughout its lifetime (Bell et al. 1997). This would result in gravitational instabilities that could generate over-dense structures oriented more or less radially and correlated with the expected dense regions where the giant planets later formed. The gas in these regions would tend to orbit faster than the dense structures, resulting in shock fronts which would raise the gas temperature within the shock. Harker and Desch suggest grain annealing is, in principle, similar to the shock-wave melting events thought to have been experienced by chondrules approximately 2–3 AU from the sun (Desch and Connolly 2002). Particles experiencing a passing shock would be accelerated and heated by thermal exchange with the hot shocked gas as well as by the absorption of thermal radiation from other grains. Immediately following the shock, the gas would quickly slow to its preshock velocity (in less than ~1 ms). Dust grains however would only be able to slow via frictional drag, causing them to experience short-lived thermal spikes lasting ~1 s. The grains would then cool by thermal emission at a rate determined by the emissivity of the grain material. Micron sized silicates in the region of 5–10 AU could have experienced spike temperatures up to a couple of hundred K above the ~1000 K silicate crystallization temperature. However, whether the short duration of these events would be enough to promote crystallization is open to debate as the calculations were based on the "silicate evolution index" (Hallenbeck, Nuth, Nelson 2000). This is an estimate of the rate at which silicate particles crystallize as a function of temperature. The index, however, is based on only one particular set of laboratory results and may, therefore, be unrepresentative of either silicates in general or of cosmic silicates in particular (Rietmeijer et al. 2002). However, the predicted 5–10 AU crystallization region is consistent with the general observation that short-period comets formed at the Edgeworth-Kuiper belt are mostly devoid of crystalline silicate, while long-period Oort cloud comets do tend to show such features. However, to explain the paucity of crystalline silicates in Edgeworth-Kuiper belt comets does require the absence of any large scale transport mechanism.

The final option is of comet crystals being relic stardust grains (Wooden et al. 2000). Observational constraints (Kemper et al. 2001), based on their non-detection in the interstellar medium, along with the possibility that at lower temperatures, pyroxene grains are difficult to detect (by either being less optically active or by having their spectral response suppressed by grain surface ice mantles), do not rule this possibility out. However, it would require significant numbers of crystalline stardust grains to survive the interstellar journey

from the circumstellar to protoplanetary environment. A range of pyroxene to olivine ratios have been observed for AGB stars where 5% to 10% of the circumstellar dust appears crystalline (Tielens et al. 1998). In the laboratory, Hallenbeck, Nuth, and Daukantas (1998) have shown that annealed Mg-rich amorphous olivine particles crystallize quicker than Fe-bearing ones, which could provide a mechanism for the bias towards Mg-rich crystal compositions. Other experiments aimed at modelling stellar condenzation also show that solids of mixed Fe-Mg-O are unlikely to form (Rietmeijer, Nuth, and Karner 1999). A stardust origin, though, would remove the need for both hot inner-nebula processing and radial transport. It would also be consistent with observations of Mg-rich crystalline silicate features in older Herbig Ae stars with cool circumstellar dust ($\leq$300 K) and cometary activity (Malfait et al. 1998), as well as debris disk systems such as β Pictoris (Waelkens et al. 1996). However, the outer solar nebula would have had to contain significant numbers of these grains to explain its abundance in comets. A complication to the stardust hypothesis, however, is whether circumstellar crystals condense out of stellar atmospheres as crystals or are themselves the result of circumstellar annealing (Demyk et al. 2000). Unfortunately, condensation models are currently unable to say anything concrete about the physical structure of the solid materials they predict (Demyk et al. 2000). Although Sogawa and Kozasa (1999) have shown crystalline grains can be produced in the outflows of high mass loss rate AGB stars by the annealing of heterogeneously condensed silicate mantles on alumina cores, that crystalline grains form by direct condensation is unlikely. Crystal growth only proceeds in relatively quiescent, slowly cooling vapors and is very slow, yielding only very small crystals. Amorphous grains entering such an environment would probably crystallize more rapidly than the crystal condensation growth rate. In a cooling vapor, the first-formed stable nuclei act as seeds for grain growth so that, given sufficient activation energy and time, condensed solids can equilibrate with the ambient environment and rearrange themselves into the lowest energy physical/chemical configurations. However, circumstellar (and solar nebular) vapors are dynamic environments and gas-to-grain condensation will likely be dominated by kinetic factors and higher vapor cooling rates. In these instances, less-ordered, meta-stable, higher-energy configurations will result. Since such freshly condensed particles will have higher internal energy, spontaneous exothermic reactions of low activation energy can occur following an energetic event such as grain collision or UV photoabsorption (Rietmeijer, Nuth, and Karner 1999). Freshly nucleated grains should therefore quickly transform into chemically homogeneous amorphous solids.

The survivability of crystalline stardust grains in the interstellar medium also poses a problem. Their apparent absence could suggest either non-trivial destruction rates or a

dilution effect by the more abundant amorphous grains. Crystalline grains could be both completely destroyed or transformed into amorphous grains. The structural and chemical evolution of grains almost certainly occurs in the interstellar medium as they will be subjected to extensive processing via grain-grain collisions, gas-grain collisions, photo-processing, and interaction with cosmic rays, ions, and shock waves. Of these, interaction with energetic ions can disrupt crystal structure and affect chemical composition. Early experiments involving the irradiation of Mg-rich crystalline olivine and pyroxene with protons, to mimic interstellar cosmic rays, showed no discernible structural effects (Day 1977). Kratschmer and Huffman (1979), however, produced amorphous silicates by the irradiation of crystalline olivine with energetic ions. Within supernova shock waves, interstellar grains can interact with atoms that have been both accelerated and ionized by the shock wave. Ion energies will depend on the details of the shock velocity, but will generally be of the order of a few keV. Calculations based on more recent experiments involving low energy He^+ implantation into crystalline, Mg-rich olivine suggest a single supernova shock wave with a velocity greater than ~400 km s^{-1} (i.e., He^+ energy above ~4 keV) would be enough to amorphize most crystalline Mg-rich olivine grains in a "standard" interstellar grain size distribution, as well as induce loss of Mg and O atoms (Demyk et al. 2001).

In summary, crystalline grains are widely assumed to result from the thermal processing of amorphous precursor grains. However, the conditions and means by which this happens are rather poorly defined. If comets are to have largely formed in the outer reaches of the early nebula from essentially unaltered amorphous interstellar dust, the question arises as to how and where the crystalline grain population formed. Understanding the physics behind the spectral features associated with crystalline comet dust will, thus, contribute not only to our knowledge of comet cosmogony but also to our understanding of the formation histories of both the solar system and the other planetary and protoplanetary systems now being discovered. To place constraints on the thermal histories of grains, both before and after comet formation, we need to better understand the properties of silicates and the processes by which they can crystallize.

Silicate Composition

The general composition of cometary silicate can be inferred from several lines of investigation.

Interplanetary Dust Particles (IDPs)

Interplanetary dust particles (IDPs) have long been known to contain components originating from comets and asteroids, as well as presolar interstellar grains that have not necessarily been processed through planetary bodies

(Brownlee 1990). Highly porous, silicate-rich IDPs have been found with large deuterium enrichments, indicating a presolar origin (Messenger et al. 1995, 1996; Messenger and Walker 1997) and a collection of IDPs is now known to be associated with Comet Schwassmann-Wachmann 3 (Messenger and Walker 1996). The presolar nature of IDPs is difficult to establish without isotopic analysis. However, pristine grains that have not suffered reheating or aqueous alteration can be identified via their porous morphologies and high Mg content (Bradley, Humecki, and Germani 1992). Circumstellar condensation models suggest that pure Mg silicates are more thermodynamically favored than Fe-bearing compositions (Grossman 1972; Petaev and Wood 1996). Pure Mg-olivine (forsterite) probably forms first, followed by pure Mg-pyroxene (enstatite) (Tielens et al. 1998). However, these are rare in the meteoritic record, constituting only ~1% by mass of unequilibrated ordinary chondrites and carbonaceous chondrites (Bradley et al 1999). The presence of Fe in meteoritic silicates is often associated with reheating events where Fe can migrate into the Mg-rich crystal or form rim structures around Mg-rich grains. Pure Mg-silicates are mostly limited to Antarctic micrometeorites and chondritic porous IDPs (CP IDPs). The latter group shows the highest level of Mg purity and, therefore, has been identified as the most pristine grains of the early solar nebula. A significant component of CP IDPs are GEMS (glasses with embedded metal sulphides, Bradley 1994a, b; Joswiak et al. 1996) which show radiation tracks indicative of exposure in the interstellar medium (Bradley, Brownlee, and Snow 1997). Certain GEMS show amorphous IR spectral resonance's similar to interstellar silicates (Bradley et al. 1998) and consequently, CP IDPs have been proposed as the basic building blocks of the solar system (Bradley, Brownlee, and Snow 1997). Another potential presolar group are Cluster IDPs (pyroxene, chondritic, porous dust particles). These appear to be morphologically unaltered, very porous, rich in Mg, crystals 0.1 to 1.0 μm in size (Bradley, Brownlee, and Snow 1997), contain GEMS, and show significant deuterium enrichments (Messenger and Walker 1997; Messenger et al. 1995, 1996, 1997).

Comet Halley Rendezvous

Estimates of the Mg:Si ratio by the PUMA-1 mass spectrometer on the Vega 1 spacecraft suggest a value somewhere between 0.5 and 1.6 (Jessberger, Christoforidis, and Kissel 1988; Lawler et al. 1989; Schultze, Kissel, and Jessberger 1997), consistent with forsterite olivine and enstatite pyroxene compositions.

Comparison of Comet Observations with Laboratory Measurements

The ~11.2 μm olivine subfeature has been observed in several comets, including comet P/Halley 1986 III (Bregman et al. 1987; Campins and Ryan 1989), Comet Levy 1990 XX, Comet Bradfield 1987 XXIX (Hanner, Lynch, and Russell

1994b), and comet Hale-Bopp (Crovisier et al. 1996, 1997; Wooden et al. 1999). Early laboratory work led to this feature being identified with the sharp feature found at this wavelength in the spectrum of Mg-rich olivine (e.g. Koike et al. 1981, 1993; Blanco et al. 1991; Jäger et al. 1998). Colangeli et al. (1995, 1996) have published fits to the 10 μm bands of several comets with 11.2 μm features using laboratory spectra for several classes of pyroxene and olivine minerals. Meanwhile, observations of comet Hale-Bopp coma grains over the region 6–45 μm (Crovisier et al. 1997) revealed a rich variety of strong emission features, particularly at longer wavelengths, attributable to forsterite olivine (Brucato et al. 1999).

These lines of investigation point to Mg-rich pyroxene and olivine compositions as the most likely form for primitive nebular silicates. Differences in the 10 μm bands of various comets have been interpreted as variations in the relative abundance of crystalline/amorphous olivines and amorphous pyroxenes (as well as the Mg/Fe ratio for olivine). For example, amorphous pyroxenes have been invoked to explain the short-wavelength rise of the 10 μm band as well as the 9.8 μm peak for comet Halley (Hanner, Lynch, and Russell 1994b; Colangeli et al. 1995). Despite both this and the presence of crystalline pyroxenes in IDPs, features due to crystalline pyroxene have not been readily observed in comets so far, suggesting either a differential in the thermal histories of olivine and pyroxene grains or that the annealing properties of pyroxene differ from those of olivine. Wooden et al. (1999) have observed a subfeature at 9.3 μm in comet Hale-Bopp, which became apparent as the comet drew closer to the sun. They subsequently attributed the feature, along with several other weaker 10 μm band features, to crystalline pyroxene with Mg = 90%. To explain the feature's absence at greater heliocentric distances, Wooden et al. suggested the high Mg content of crystalline pyroxene lowers its optical activity, keeping the grains cooler, and thus, harder to detect.

The Silicate Crystallization Problem: Experimental Objectives

Comparisons between comet and laboratory spectra suggest cometary silicates are best represented by silicates intermediate of amorphous and crystalline (Hallenbeck, Nuth, and Daukantas 1998). This point is important because, as a structure probing tool, the solid state IR spectrum samples a slightly different physics between amorphous and crystalline materials. Although IR features arise from atomic vibrations, in crystalline solids, the vibrational excitations are associated with plane waves characterised by a frequency and a wave vector. For crystal lattice vibrations, momentum conservation is important, and only a small number of all possible lattice vibrations are optically active. This yields a spectrum comprising a series of sharp bands. Structural disorder, however, localizes the vibrations, and they can no longer be

treated as plane waves. As a direct consequence of the reduced structural symmetry, most vibrational modes are, therefore, optically active. So, even though the vibrational density of states (which reflects nearest neighbour interaction) for an amorphous material differs little from its crystalline counterpart, it is reflected to a much greater extent in its IR spectrum. The dispersion in bond angles and bond lengths is also greater in amorphous solids and yields a wider range of bond strengths, and hence, vibrational frequencies. The fundamental absorption feature is, therefore, much broader than the corresponding crystalline one and lacks fine structure. As the atomic structure becomes more regular (e.g., during annealing), the bond length and angle dispersions decrease, and the main absorption band shrinks in width while narrow subfeatures form. The spectrum, thus, becomes less representative of the vibrational density of states and more representative of the existence of the structural symmetry conditions necessary for plane wave propagation.

For amorphous silicates, the IR spectrum provides information, particularly at 10 μm, about the short range structure (i.e., the various SiO_n species present), while in the crystalline state, it can also convey information on the existence of longer-range correlations. This begs the question of how intermediate spectra are to be interpreted. Without knowing how the material structure evolves as a function of the annealing conditions, saying anything concrete about what the spectrum represents is difficult. Without corroborating evidence, the identifying of relatively weak sub-features in the observational data with the intense sharp peaks present in crystalline reference spectra does presuppose, somewhat circularly, that the observed sub-features actually originate solely from the presence of bulk crystalline structures. Detailed consideration of this issue is conspicuously lacking in the astrophysical literature. In addition, the terms mineral, glass, amorphous, crystalline, and indeed silicate are freely applied to laboratory and cosmic materials alike. However, each has only limited application and to the non-specialist, may infer characteristics that are not necessarily wholly appropriate (c.f., Jäger et al. 1994). The objectives of the present work are, therefore, to explore the relation between spectral and structural evolution for laboratory analogues. We have, thus, combined IR spectroscopy with the structure probing technique of synchrotron X-ray powder diffraction (SXRD). The SXRD measurements are novel in that data collection occurs during annealing through the use of an in situ furnace.

EXPERIMENTAL DETAILS

Sample Manufacture and Preparation

Over the years, simulant grains have been manufactured using a variety of techniques (e.g., smokes, laser evaporation, gas phase condensation) aimed at producing particles via

processes that mimic certain aspects of grain formation. While undoubtedly useful, in terms of understanding the underlying fundamental properties of silicates, the samples they yield can be far from ideal. They are often highly disordered both structurally and chemically and can contain significant fractions of oxides such as SiO, MgO, and FeO, as well as chemically separated Mg and Fe metal units. While such defects are likely to be present in freshly nucleated grains, for our purposes, we have selected a simpler system that mimics the bulk compositional component of comet dust. Our amorphous starting material was produced by gel desiccation (Sabatier 1950; Day 1974, 1976a, b), which has the advantage of yielding a silicate with an evenly dispersed composition and a well established Si-O tetrahedral environment. Samples produced by this method were also among the earliest laboratory silicates studied from an astronomical view point (Day 1974, 1976a, b; Steel and Duley 1987, Thompson, Evans, and Jones 1996; Thompson and Tang 2001). A hydrated solid precipitate is formed in solution according to the following basic reaction,

$$Na_2SiO_3 + MgCl_2 \rightarrow (MgSiO_3)_{solid} + 2NaCl \qquad (1)$$
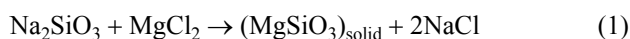
and prepared according to the following steps:

1. 0.1 M solutions of the soluble metal salts $MgCl_2$ and Na_2SiO_3 were mixed in the correct stoichiometric ratio required to produce $MgSiO_3$.
2. The white suspension thus formed was left to settle for two days. The excess liquid was decanted off and the suspension centrifuged and washed with distilled water to remove the soluble sodium salt. This cycle was repeated three times.
3. The resulting gelatinous precipitate was then dried in air over a hot plate (100–150°C) to yield irregular lumps of a white glassy-looking solid, which was ground to produce a fine grained powder.

SEM imaging and pre- and post-annealing showed a distribution of particle sizes ranging from a few μm up to several hundred μm with an average of ~100 μm. During annealing, there was a substantial reduction in sample mass but no apparent change in size distribution. Our particles are probably somewhat large compared to the likely size of the cometary grains responsible for the 10 and 20 μm bands (Brucato et al. 1999), however, it is unlikely that this is a significant factor in determining our results as we are concerned primarily with internal structural changes which are unlikely to be affected by particle size. Although Rietmeijer et al. (2002) have observed a size dependency for annealed smokes, their particle size range was significantly smaller. We recognize, however, that this deserves closer scrutiny and plan to address this in future work.

Synchrotron X-ray Powder Diffraction (SXRD)

SXRD measurements were performed on station 2.3 of the Daresbury Laboratory Synchrotron Radiation Source (SRS, Munro 1997). The two circle (θ and 2θ) diffractometer is designed for high resolution powder diffraction (Collins et al. 1992). A water cooled Si (111) channel-cut single crystal delivers monochromatic X-rays in the range of 0.7–2.5 Å. For non-crystalline materials, there is a trade off between the short X-ray wavelengths needed to maximise reciprocal wave-space sampling (see Equation 5) and the need for high photon flux to minimise detector integration times. For in situ measurements on dynamic systems, there is also a need to collect data rapidly, as well as a need to collect as much structural information with as high a signal-to-noise ratio as possible (i.e., wide angular ranges and long integration times). A wavelength of 1.2995 Å, calibrated against a high quality crystalline Si reference powder, was chosen as a good compromise between peak incident flux and low wavelength. The step size of the 2θ detector arm was set to 0.01° and a 2θ range of 10–60° allowed the capture of a reasonable amount of structural data within ~75 minutes per scan using 1 s integration times per step.

The SRS X-ray diffraction facilities operate various in situ sample environments covering the range ~10 to ~1700 K and include a RF induction furnace (Tang, Bushnell-Wye, and Cernik 1998). Its operational range is 290–1700 K with, for example, a heating response time of 30 s for a target temperature of 800 K and ±1 K stability, achieved within a few minutes. The sample crucible is molybdenum and a 1 mm deep by 15 mm diameter pressed platinum former is placed on the crucible to hold the sample, preventing a chemical reaction between the sample and crucible. The sample is heated via a water-cooled 2 kW RF Cu coil regulated by a Eurotherm 900 controller. Sample temperature is monitored via a Pt-rhodium thermocouple at the sample holder. The furnace assembly is enclosed in a stainless steel body mounted on the θ-circle axis, with the sample co-located at the center of the θ-circle and aligned with the incident X-ray beam. This enables the system to conform to Hart-Parrish diffraction geometry (Hart and Parrish 1986), making it insensitive to changes in sample height, which is essential, as small sample movements are inevitable during heating. Incident and diffracted X-rays pass through 50 μm thick kapton windows in the furnace body. Finally, the diffracted beam passes through a parallel foil collimator on the 2θ-circle detector arm to an enhanced dynamic range scintillation counter. Scans are normally performed by coupled rotation of the θ and 2θ axes, but to prevent the sample falling from the holder at high angles, the θ-circle was fixed at 10° with measured intensities corrected according to standard method. To reduce possible reaction between sample and atmospheric gases, the furnace was evacuated to below ~10^{-2} mbar. Annealing temperature was approached in progressively smaller steps to avoid overshoot, with ramp time to 1000 K taking ~5 min. Data collection began a few minutes later, once the sample temperature stabilized.

IR Spectroscopy (IRS)

For cometary grains, any scattering contribution to the 10 and 20 μm absorption band profiles is negligible since the 10 μm band is also seen in emission when many comets are <1 AU from the sun (Ney 1982). The most straightforward method of measuring absorption spectra is to mix the sample with an IR transparent medium, such as KBr powder, and compress it into a small solid pellet. Transmission measurements are then made using a suitable IR source. While this technique is common in laboratory astrophysics (Borghesi, Bussoletti, and Colangeli 1985; Bussoletti et al. 1987), annealing can not be done in situ. For this, we used a CTF 12/65 Carbolite furnace, comprising a heated alumina tube, ~700 mm in length by 75 mm in diameter, with the sample placed on an alumina plate in the tube center. Temperature was monitored by a NiCroSil/NiSil thermocouple at the sample plate. The furnace was evacuated, and annealing began once the pressure fell below 10^{-4} mbar (remaining between 2×10^{-5} and 5×10^{-5} mbar following an initial rise at the beginning). The furnace has no cooling system, so to further minimize sample-atmosphere reaction, it was left to cool to room temperature before removing and pressing the sample into pellets. Given the differences between furnaces, we defined an annealing profile for the IRS measurements to complement the SXRD profile (Fig. 1). The furnace is switched on at t = 0 and the sample temperature rises to the set-point temperature, T_{set} (measured in °C), which is then maintained for $\Delta t = t_3 - t_2$, with furnace switch-off at t = t_3. It then cools naturally and at t = t_4 falls to 85% of T_{set}. Annealing time is, thus, defined as the time spent above 85% of the set-point temperature, i.e., $t_{anneal} = t_4 - t_1$. Although 85% may appear arbitrary, its actual value should not have any adverse bearing on our results since we use it only to define two basic periods, t_{short} (2–4 hr) and t_{long} (20–24 hr). Spectra were recorded using a Perkin-Elmer Spectrum 2000 FT-IR spectrometer equipped with a single beam Michelson interferometer covering the range of 1.28–25 μm, a KBr beam splitter and a Fast Recovery Deuterated TriGlycine Sulphate (FR-DTGS) detector. A wire coil at 1350 K provided the IR source. Spectral resolution was set to 4 cm^{-1}, sufficient to resolve narrow-width, solid-state, fine structure features. Measured interferograms were transformed directly using the manufacturer's proprietary FFT software.

RESULTS

SXRD of the Initial Amorphous Silicate

Introductory texts on X-ray diffraction usually start with a derivation of the well-known Bragg equation, $\lambda = 2d\sin\theta_B$, using the concept of constructive/destructive interference of waves, of wavelength λ, reflected from uniformly spaced lattice planes distance d apart. The angle at which constructive interference occurs is the Bragg angle θ_B. In crystals, the regular arrangement of atoms allows the
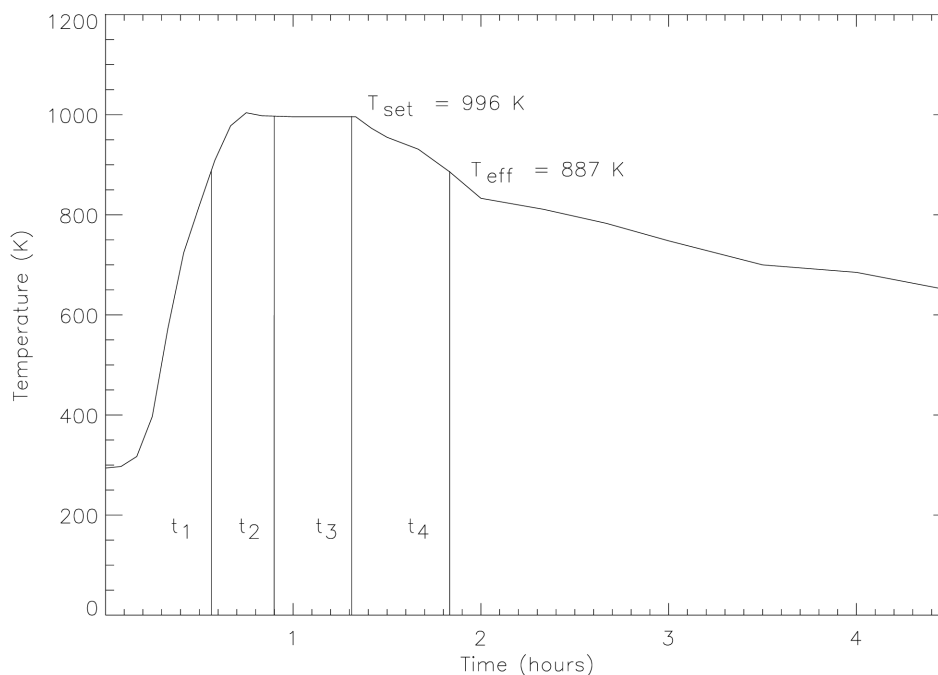

Fig. 1. Annealing temperature profile for samples prepared for IR spectroscopy measurements: T_{set} is the target set point temperature and T_{eff} is the effective temperature defined as 85% of T_{set} (measured in °C). The furnace is turned on at time t = 0, T_{eff} is reached at t = t_1 and T_{set} reached at t = t_2. At t = t_3 the furnace is switched off and allowed to cool and again reaches T_{eff} at t = t_4. The annealing time is defined as the time spent above T_{eff}.

identification of many such planes, each described by Miller indices (*hkl*). Unfortunately, for amorphous materials, there are two drawbacks to this. First, it is a fundamental explanation of interference effects solely in terms of crystalline structure and, therefore, misleading regarding non-crystalline materials. Second, θ_B only conveys information about the angle at which the measured intensity will be non-zero. The Bragg equation, therefore, contains little to aid the determination of amorphous structures. Additionally, crystals are described by symmetries and a few atomic positions. For non-crystalline materials, complete structural specification would mean a separate coordinate for every atom and would apply only to a given sample, as another similarly randomized structure would, by definition, have a different arrangement. In that sense, the amorphous state is not unique; it does not necessarily represent a minimum-energy configuration, and structural information can only be statistical and less specific.

The measured intensity, *I(Q)*, of X-rays scattered by an amorphous material comprising N molecules per unit volume, as a function of reciprocal wave-space scattering vector, *Q*, is determined by the following expressions:

$$I(Q) = NF^2(Q)S(Q) \tag{2}$$

$$F(Q) = \sum_{m=1}^{N} f_m(Q)\text{sinc}(Qr) \tag{3}$$

$$S(Q) = 1 + \frac{N}{V}\int 4\pi r^2 g(r)\sin c(Qr)dr \tag{4}$$

where *F(Q)* is the spherically symmetric Fourier Transform of a single molecular unit obtained by summing the Fourier Transforms of its individual atoms (represented by their atomic scattering factors f_m). *S(Q)* is the inter-molecular interference term and represents a modulation of $F^2(Q)$ due to the relative structural arrangement of the N molecules (here a "molecule" is an assembly of atoms in close configurational association without any implication of bonding). *S(Q)* is a function of the real-space molecular radial distribution function, *g(r)*, which is the probability of finding a molecule at distance *r* from an arbitrary origin. Arrangements of molecules are never truly random as each excludes all others from its immediate space, so real amorphous solids are not random assemblages. Thus, even without long-range order, there will always be statistical short-to-medium range order. Additionally, the dispersion of inter-molecular bond angles will tend to peak around the corresponding crystalline value. The modulation of $F^2(Q)$ by *S(Q)* also means the measured intensity between peaks is usually non-zero. Finally, the scattering wave vector, $\underline{Q}$, defines the extent to which the material's reciprocal wave-space is sampled, as a function of scattering angle and wavelength:

$$Q = \left|\underline{Q}\right| = \frac{4\pi\sin\theta}{\lambda} \tag{5}$$

Fig. 2 shows SXRD data for our unprocessed amorphous sample at ambient temperature. There are several broad features typical of non-crystalline scattering located approximately at 10°, 20°, 30°, 50°, and 60° 2θ. To understand these, we first consider the molecular contribution. The square of Equation 3 can be rewritten in its discrete Debye form as:

$$F^2(Q) = \sum_m \sum_n f_m f_n \frac{\sin Qr_{mn}}{Qr_{mn}} \tag{6}$$

Here, we perform a double summation over *m* atoms, with relative separations r_{mn}. For SiO_4, the O-O bond length depends on the Si-O bond length, $r_{O\text{-}O} = (\sqrt{8/3})r_{Si\text{-}O}$, with $r_{Si\text{-}O} \sim 1.6$Å. Si and O f-factors were calculated according to Waassmaier and Kiferl (1995). The result is shown in Fig. 3. There are two weak humps at ~35° and ~55° 2θ, but the match to the measured pattern is poor. The internal structure of the tetrahedra clearly does not contribute substantially to the diffraction features.

We now include *S(Q)* and a simple radial distribution function (Table 2) for basic tetrahedral clusters (T_n-species, see Fig. 4). We assume the locations of tetrahedra are determined only by the inter-tetrahedral bond, rather than random packing. The results are shown in Figs. 5a, 5b, and 5c. The features at ~35° and ~57° have shifted towards 30° and 60° and decrease in relative strength for clusters $>T_1$, while a weak feature at ~18° appears for clusters $>T_2$, shifting to lower angles as cluster size increases. A low angle peak occurs for T_1 and T_2, again dependent on cluster size. Qualitatively, the calculations account for most of the features in the measured pattern, suggesting it is largely determined by the nearest neighbour tetrahedral connectivity. As we do not know the relative abundance of T_n, the measured   pattern will be some weighted sum of contributions from each species.

To include larger clusters with two or more shells to improve the fit would require making assumptions about the inter-tetrahedral bond angle dispersion and cation distribution (i.e., cluster groupings). However, as our basic model does not account for the appearance of all the structure in the measured pattern (e.g., the feature at ~20°), it is likely that some medium-range structure also exists. We can expect some tetrahedra to form localized sheet and chain structures. In layer forming silicates, the intra-layer atomic bonding is stronger than the inter-layer bonding, so there are often alternative ways of stacking layers relative to each other. If either the same stacking choice is used or regular repeating sequences employed, regular crystal structure results. However, when the stacking arrangements are close in energy, deviations are likely so that except for the layer separation distance, there is no regularity in the stacking order. This affects the appearance of the diffraction pattern. If, for example, the layers are stacked parallel to the (00*l*) lattice direction, then reflections of type 00*l*
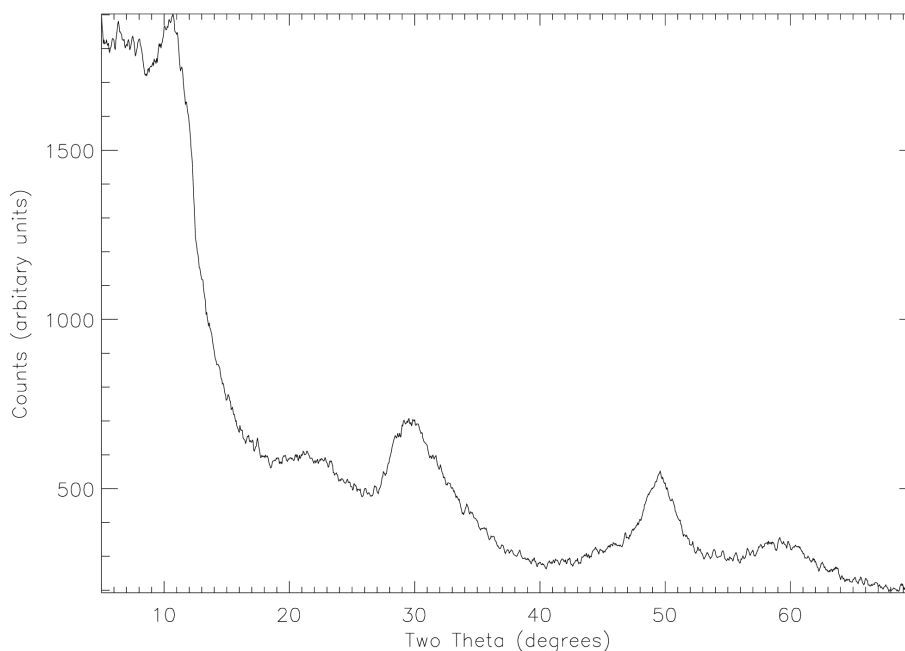
Fig. 2. SXRD pattern recorded for the amorphous starting material at room temperature.
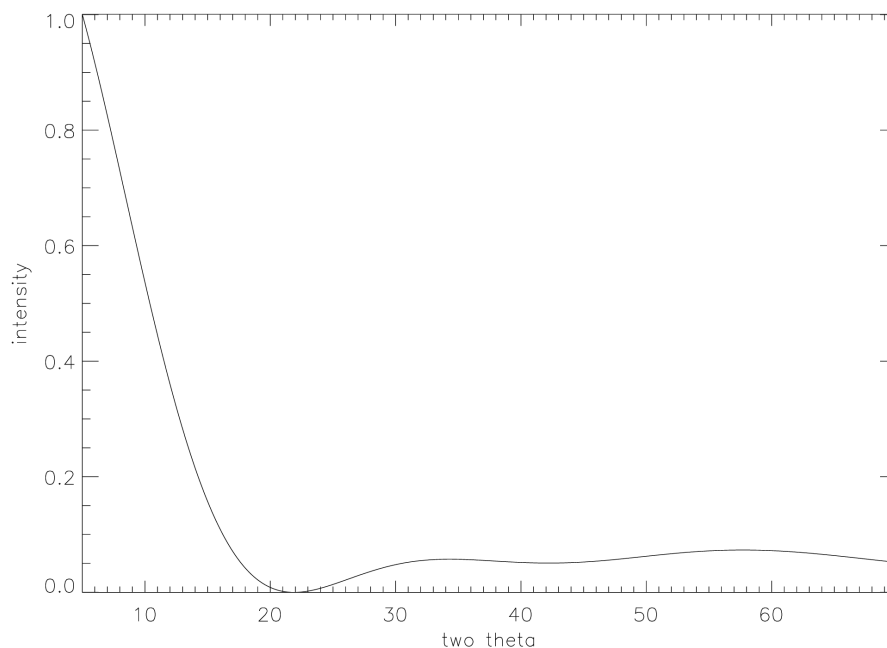

Fig. 3. Normalized theoretical X-ray scattering intensity calculated for a single SiO_4 molecule.

will appear quite normal (i.e., crystalline) because of the stacking d-spacing. However if the lateral displacements of the layers are totally irregular, it is impossible to define planes with the more general indices $hk0$ or hkl. So, apart from the $00l$ peaks, the only other observable effects will be those due to any 2-dimensional in-plane regularity. However, these will not be confined to specific Bragg angles, and instead of sharp diffraction features, will produce diffuse asymmetric bands with a sharp cut-off on the low-angle side and a gradual high-angle decay (Whittaker 1981). These are characterized by two indices, hk, and the low-angle cut off lies close to the position that would otherwise be occupied by the crystalline $hk0$ reflection of the corresponding 3-dimensionally ordered structure. The feature at ~30° 2θ is asymmetric with a sharp low-angle rise and gradual high angle decay. The 2θ rise begins at ~27° 2θ, giving an interlayer d-space of ~2.70 Å and

Table 2. Idealized radial distribution function for first coordination shell of SiO_n molecules.

g(r)	r(Å)
0.0	$r \leq r_{Si-O}$
$n(r/r_{Si-O} - 1)$	$r_{Si-O} < r \leq 2r_{Si-O}$
$n(3 - r/r_{Si-O})$	$2r_{Si-O} < r \leq 3r_{Si-O}$
0.0	$r > 3r_{Si-O}$

corresponds to the forsterite, Mg_2SiO_4, (130) lattice spacing. The absence of sharp peaks indicates that the stacking of these layer-forming components is not ordered. The feature at 60° 2θ similarly corresponds to the forsterite (170) inter-layer distance of ~1.35 Å.

In Situ SXRD at 1000 K

Using the RF furnace, we performed measurements on the amorphous sample at 1000 K. Data were collected for 19.5 hours. During this time, crystal structure evolved (Fig. 6) and, by the end, appeared as a well-developed crystalline pattern upon an amorphous background. The broad features in the amorphous pattern at ~30° and 50° 2θ decreased in width during the first scan, becoming more symmetric. The crystalline component had begun forming after ~2 hr and after ~5 hr had reached its full extent (i.e., no new peaks). From that point, neither the crystalline nor amorphous

component changed. At this temperature, the crystalline structure rapidly establishes itself, at the expense of the amorphous component, but then structural evolution appears to stall.

Using reference data (based on the Joint Committee for Powder Diffraction Standards database), the crystalline pattern was identified as forsterite (Mg_2SiO_4), with no match being obtained for crystalline enstatite ($MgSiO_3$). The identification in the unprocessed sample of disordered forsteritic components suggests that the initial crystallization of Mg_2SiO_4 proceeds around these units already present in the sample. Since amorphous silicates generally posses a distribution of SiO_n (Gurman 1990), it is likely that the initial ordering of Mg_2SiO_4 involves only those units that do not share O atoms, as reorganizing inter-linked tetrahedra will necessarily entail breaking and reforming bonds.

In Situ SXRD above 1000 K

Since the formation of crystalline forsterite from amorphous $MgSiO_3$ was unexpected at these temperatures, the possibility remained that the stalled forsterite structure represented a transitional phase. To test this, we increased the temperature to 1031 K and annealed the sample for an additional 24.5 hr. During this time, the pattern did not vary significantly from that of 1000 K. Further processing at 1043
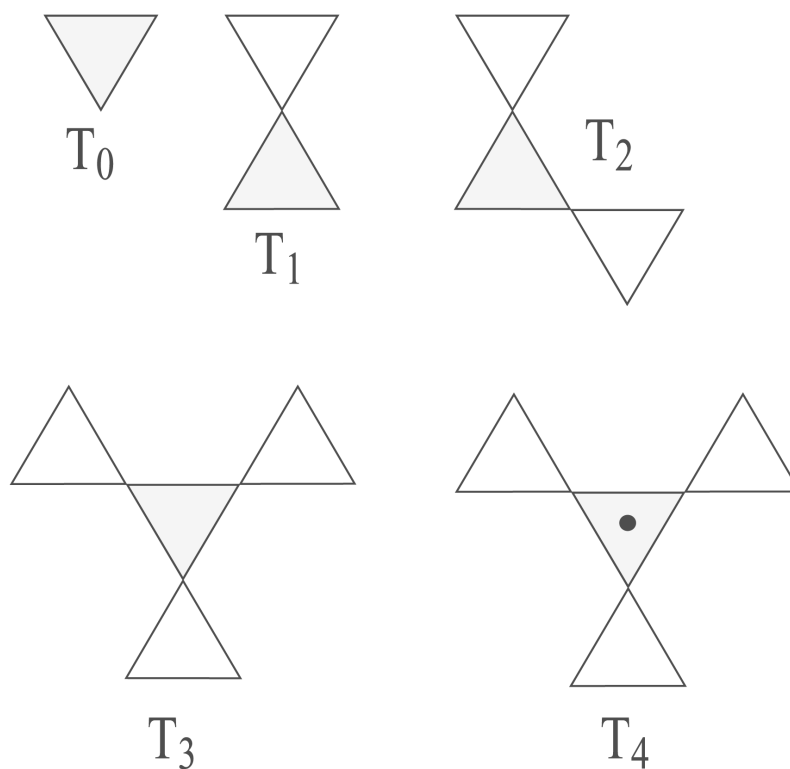

Fig. 4. Basic silicate tetraheral clusters denoted as T_n, where n is the number of tetrahedra coordinating the central molecule (shown shaded). Cluster size is thus n + 1 and the black spot for T_4 indicates the presence of a tetrahedron located out of the page. Since the radial distribution function is spherically symmetric, it is insensitive to the particular choice of arrangement for the T_1, T_2, and T_3 species.

K for 24 hr gave the same result. The temperature was then raised over 5 hr through 1083 K, 1113 K, and 1143 K with no significant change to either amorphous or crystalline components. Finally, the temperature was raised to 1173 K and the sample annealed for a further 14.5 hr. Only then did it show evidence of further structural growth. After 5–6 hr the pattern underwent rapid modification, with changes in the profile of the amorphous component and a sharpening and

growth of existing crystalline peaks, as well as the formation of new ones. Analysis of the post-stall SXRD data again identified the majority of crystalline features as forsterite, though some remained unidentified. We could not extend annealing further due to the limitations of synchrotron beam time allocation. If forsterite is an intermediary step between amorphous and crystalline end states of our sample, it would appear to be a relatively stable one.
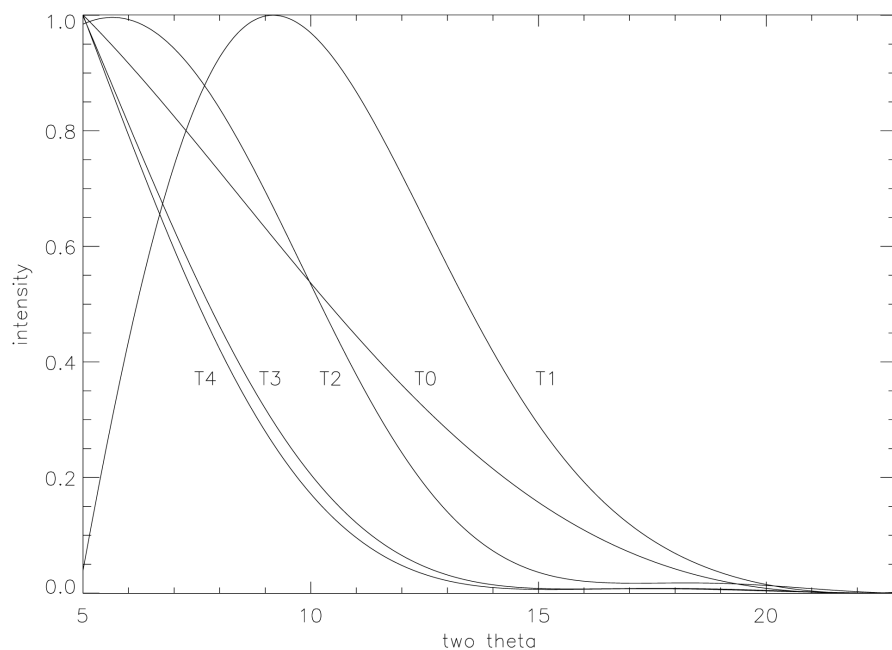

Fig. 5a. Calculated low-angle normalized X-ray scattering intensities for T_n silicate clusters.
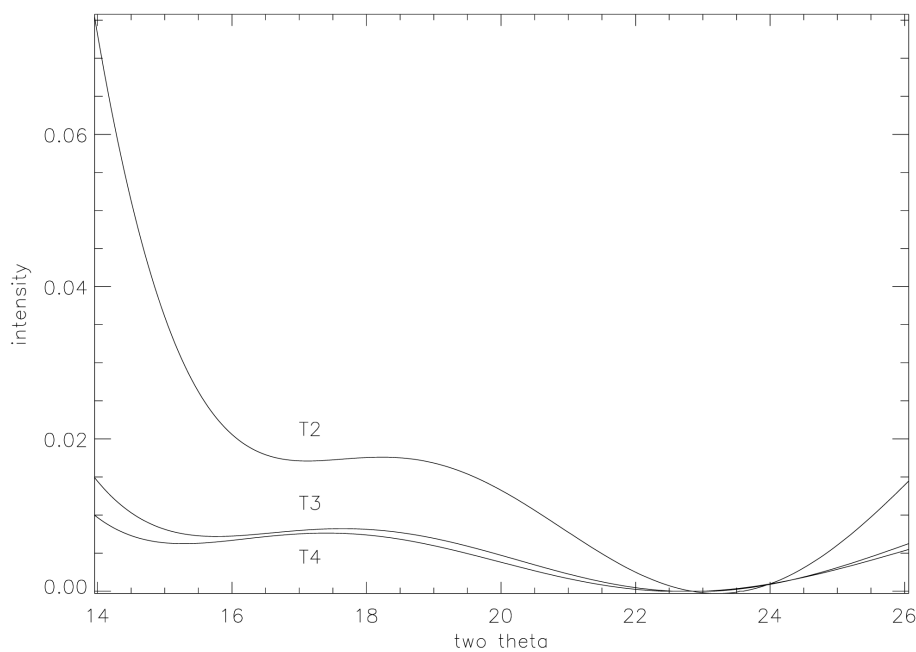

Fig. 5b. Calculated mid-angle normalized X-ray scattering intensities for T_n silicate clusters.
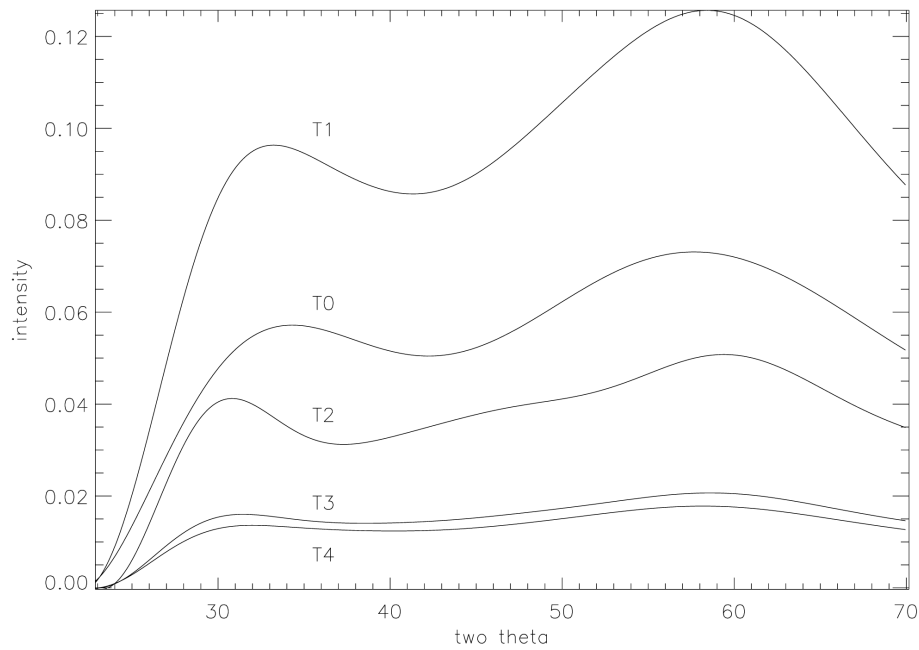
Fig. 5c. Calculated high-angle normalized X-ray scattering intensities for T_n silicate clusters.
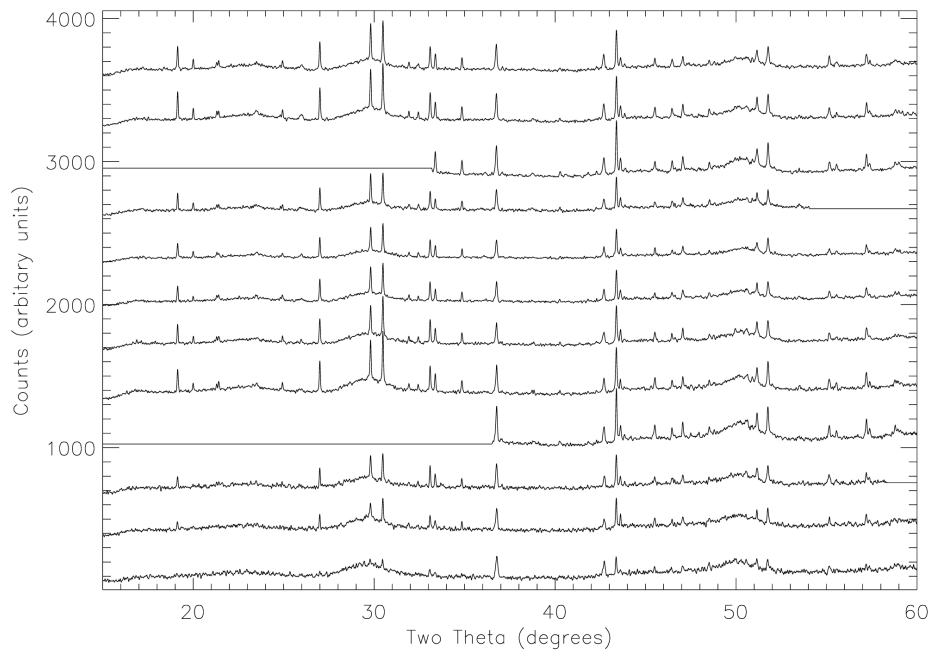

Fig. 6. SXRD patterns collected at 1000 K. The bottom pattern is the first scan while the top pattern is the final scan collected 19.5 hr later. The straight line sections are where the synchrotron beam was unavailable due to synchrotron refills.

The Missing Crystalline Enstatite Problem

Although forsterite is the dominant crystalline phase at both the high and low ends of our temperature range, we cannot ignore the possibility of enstatite existing as a very disordered or very dilute crystalline phase. For highly disordered crystalline phases (depending on the nature of the disorder), diffraction peaks either become broader and less intense or remain sharp but with greatly diminished intensities (Hukins 1981). In either case, the short integration times sufficient to give good signal-to-noise statistics for well ordered crystals can be inadequate for detecting features from such systems. For crystals, the form of $S(Q)$ embodies the symmetry arrangements of the crystal lattice and has the

effect of amplifying peak intensities by concentrating the scattered intensity into a few selected regions of Q-space (i.e., the Bragg reflections) while remaining zero everywhere else. In disordered systems, not only do the peaks in S(Q) decrease significantly and their breadth increase, but S(Q) becomes non-zero in the rest of the Q-space. Thus, for mixed ordered and disordered samples, the short integration times used to detect the intense peaks of the ordered phase can cause the disordered phase to go undetected relative to the background signal. Unfortunately, in time-resolved experiments, short integration times are essential for observing dynamic changes. The possibility, thus, remained that undetected enstatite structures may still exist in the sample.

To test this, we summed the 1000 K SXRD data to give an effective integration time of 12 s per point and obtained peak positions for all visible Bragg peaks. Rather than compare these to search-match reference data, we employed an indexing method (Hwang and Tien 1996) that takes as its input the initial lattice parameters of the likely crystalline unit cell and its crystallographic type. Theoretical d-spaces for all possible lattice planes are then calculated using standard crystallographic formulae. A global function, E, is minimized based on the sum of the squares of the differences between observed and calculated peak positions for subsequent sets of Monte Carlo generated lattice parameters, based on the initial supplied values. The error associated with the observed peak position is used to determine whether it matches a calculated one, and hence, whether it belongs to the crystalline phase of interest or not. If not sufficiently close, the observed peak is rejected as likely belonging to another phase. The degrading influence of rejected peaks is eliminated by excluding their contribution to the calculation of E. Thus, a best fit to the measured peak positions, based on a minimum E, is output along with refined lattice parameters and a list of rejected peaks. The procedure was performed using the XRAYSCAN code (CCP14 X-ray diffraction program library).

Initial lattice parameters were taken from published data for forsterite (orthorhombic unit cell), three typical sets of orthorhombic enstatite parameters, and one set of clinoenstatite (monoclinic unit cell). Unfortunately XRAYSCAN does not handle monoclinic structures and the fits reported here for clinoenstatite are based on calculated versus observed peak differences without refinement. The search for enstatite is complicated by its lattice parameters showing wide variation due to enstatite, assuming either monoclinic or orthorhombic unit cells and orthorhombic enstatite forming single- or multi-linked chain structures. The results for the 1000 K summed data are shown in Table 3 and initial and refined parameters in Table 4. Forsterite gives the best fit to all but one of the peaks. Two of the orthorhombic enstatite structures produce fits to some of the peaks already fitted by forsterite, while the third gave no fits at all. None of the orthorhombic enstatite fits were unique and all gave lattice parameters smaller than the initial (ambient temperature) values. Only forsterite showed an increase in cell dimension as would be expected for a material at a substantially elevated temperature. Interestingly, monoclinic enstatite gave a match to the single peak rejected by the forsterite fit. However, the d-space difference between observed and calculated peak position is about an order of magnitude greater than those established for the other peaks fitted by forsterite. This could be due to the non-refinement of the monoclinic cell parameters not reflecting the thermal expansion of the material. The feature, however, was weak even in the summed data, and its position may be subject to larger error. In the individual scans, it is only visible as a weak background feature in the last few, implying it developed late during annealing. If this is due to monoclinic enstatite, it would have to represent an ultra-dilute or highly disordered structure.

As expected, summing the data for stall temperatures above 1000 K produced patterns that were no different. At 1173 K, however, the sample had evolved further, so we applied the procedure to these data (Table 5). Again, forsterite gave the best fit to the majority of peaks and, where enstatite and forsterite fits coincide, the forsterite fit tends to be better. However, there are several peaks that are only matched by one or other of the 4 forms of enstatite, though most of these are very weak even in the summed data. Thus, although the change in structure is still dominated by forsterite, some dilute crystalline enstatite may also form, but with no overall unit cell appearing to be adopted, suggesting the structures may be highly localized.

IR Spectroscopy

For the t_{short} and t_{long} annealing times at 1000 K, initial measurements showed a high degree of fine structure in both 10 and 20 μm bands. Although differences existed, they were too minor to allow us to draw concrete conclusions. To better observe spectral development, we performed additional measurements at the lower temperatures of 873 K and 970 K. Usually, IR spectra are normalized according to sample mass. However, certain problems associated with determining the precise mass reduction during annealing made this difficult. Instead, we scaled the lowest and highest points of each spectrum in the range of 8–24 μm to the interval 0 to 1. We selected 8–24 μm because silicates exhibit both their main absorption features and an absorption minimum in this region. Although this does not allow for specific quantitative inter-comparisons of features, it does provide an easy means of seeing the spectral changes induced by annealing.

In the unprocessed sample, both the 10 and 20 μm bands are free of sub-features, although there is a visible shoulder at ~11.2 μm. This was also the first part of the 10 μm band to develop into a feature during annealing and corresponds to the olivine SiO_4 asymmetric stretch mode. Its presence in the unprocessed sample corroborates the identification of pre-

Table 3. Fits to summed SXRD data at 1000 K.

Observed peak positions		Forsterite	Ortho enstatite 1	Ortho enstatite 2	Ortho enstatite 3	Clino enstatite
2θ (deg)	d-space (Å)	d_{obs}-d_{cal}	d_{obs}-d_{cal}	d_{obs}-d_{cal}	d_{obs}-d_{cal}	d_{obs}-d_{cal}
19.1401	3.90819	−0.00014	–	–	–	–
20.0001	3.74174	−0.00075	–	0.00054	–	–
21.3001	3.51577	−0.00046	–	–	–	–
21.4001	3.49954	−0.00167	–	–	–	–
23.5202	3.18795	–	–	–	–	0.01911
24.9302	3.01026	−0.00053	–	–	–	–
26.0003	2.88837	0.00003	–	–	–	–
27.0003	2.78328	0.00010	–	–	–	–
29.8103	2.52605	0.00032	–	0.00070	–	–
30.4904	2.47100	0.00045	–	–	–	–
31.9204	2.36299	−0.00009	–	–	–	−0.00039
32.4504	2.32541	0.00023	–	0.00108	–	−0.00926
33.0904	2.28165	−0.00022	–	0.00164	–	−0.00076
33.3804	2.26239	0.00006	–	0.00219	–	–
34.8505	2.16973	−0.00037	–	–	–	–
36.7605	2.06059	−0.00531	–	−0.00077	–	–
38.8105	1.95562	−0.00159	–	–	–	–
40.2806	1.88705	0.00079	–	–	–	–
41.8306	1.82009	0.00047	–	–	–	–
42.2906	1.80119	0.00015	–	−0.00022	–	0.00005
43.3806	1.75803	−0.00038	–	−0.00148	–	0.00039
43.6107	1.74920	−0.00027	–	–	–	–
43.8607	1.73972	0.00074	–	−0.00061	–	–
45.5207	1.67947	0.00001	–	–	–	–
46.4507	1.64765	−0.00030	–	−0.00106	–	–
47.0607	1.62749	0.00017	–	0.00115	–	–
48.5208	1.58135	0.00000	–	–	–	–
51.7708	1.50510	−0.00023	–	−0.00049	–	–
51.7708	1.48830	0.00029	0.00026	–	–	–
53.5109	1.44330	0.00019	–	0.00079	–	–
55.1609	1.40337	0.00033	−0.00017	–	–	–
55.5609	1.39406	0.00000	0.00064	–	–	−0.00052
57.2010	1.35732	−0.00022	–	–	–	–
57.3910	1.35321	−0.00014	–	–	–	–

Table 4. Initial and refined lattice parameters for forsterite and various enstatite unit cells.

	Initial lattice parameters (Å)			1000 K refined values			1173 K refined values		
	a	b	c	a	b	c	a	b	c
Forsterite	4.75	10.19	5.97	4.775	10.276	6.019	4.7837	10.2993	6.0334
Enstatite 1	4.78	4.933	6.902	4.204	4.466	6.773	4.8677	4.7601	6.9965
Enstatite 2	18.21	8.8	5.17	17.724	7.752	4.878	17.7123	7.7447	4.8612
Enstatite 3	9.25	8.25	5.32	–	–	–	8.8019	7.8452	4.8965
Clinoenstatite (β = 108.335°)	9.61	8.81	5.17	–	–	–	–	–	–

existing proto-forsteritic structures from the amorphous SXRD data. Comparing the spectra for the two annealing periods, the 10 μm band features appear to develop both as a function of time and temperature (Fig. 7). The 20 μm band features, however, appear to evolve mostly as a function of temperature (Fig. 8). Although no direct correlation exists between the 20 μm band features and any physical parameter related to the structure of silicates (McMillan 1984a, b), its origin in the inter-tetrahedral bending vibration means that changes in this band are indicators of change in the silicate network (Nuth and Hecht 1990). At 873 K, there are three broad features at 19.7, 21.5, and 23.7 μm, while at 970 K the middle one of these appears to split, giving four features at 19.7, 20.9, 21.6, and 23.8 μm. Finally, the 1000 K t_{short} spectrum shows seven features at 19.6, 20.8, 21.7, 22.7, 23.4, 23.7, and 24.5 μm, with possible weak shoulders at 24.1 and 22.0 μm. Unlike the previous spectra, the 20 μm region of the 1000 K t_{long} spectrum shows evidence of temporal evolution in that there appears to be a weak modulation and possible further splitting of features. Comparing feature positions with

Table 5. Fits to summed SXRD 1173 K data.

Observed peak positions		Forsterite	Ortho enstatite 1	Ortho enstatite 2	Ortho enstatite 3	Clino enstatite
2θ (deg)	d-space (Å)	d_{obs}-d_{cal}	d_{obs}-d_{cal}	d_{obs}-d_{cal}	d_{obs}-d_{cal}	d_{obs}-d_{cal}
15.96	4.68027	–	–	0.00753	–	–
16.81	4.44519	–	–	–	–	–
17.24	4.33510	0.00345	–	–	–	–
18.12	4.12619	–	–	–0.00890	–	–
19.10	3.91630	0.0059	–	–	0.00631	–
19.42	3.85237	–	–	–0.00828	–	0.00704
19.96	3.74916	–0.00074	–	0.00363	0.00737	–
21.27	3.52068	0.00172	–	–	–	–0.00387
21.37	3.50439	0.00043	–0.00615	–	–	–
22.01	3.40368	–	–0.00039	–	–	–
23.47	3.19465	–	–	–	–	–
24.88	3.01622	0.00047	–	–0.00097	0.00457	–
25.95	2.89384	0.00121	–	–	–0.00235	–0.00367
26.94	2.78936	–0.00020	–	–	–	–
29.74	2.53186	–0.00014	–	–0.00154	–	–
30.41	2.47734	–0.00055	–	0.00107	–	–
31.86	2.36732	0.00086	–	–0.00199	–	–
32.38	2.33030	–0.00046	0.00186	–	–	–0.00437
33.02	2.28635	0.00003	–	–	–	0.00394
33.30	2.26767	–0.00041	–	–	–	–
34.79	2.17336	0.00006	–	–	–	–
36.57	2.07093	–	–0.00094	–	–	0.00193
40.18	1.89155	0.00037	–	–0.00005	–	–
41.74	1.82384	0.00078	0.00052	–0.00021	–	0.00008
42.47	1.79390	–	–	–	–	0.00978
43.30	1.76112	0.00007	–	–0.00024	–0.00075	–0.00074
43.53	1.75226	0.00015	–	0.00062	–0.00076	–
45.41	1.68332	–0.00046	0.00056	–	0.00038	–
46.35	1.65101	0.00002	–	–0.00075	–	–
46.95	1.63108	0.00020	–	–	–0.00055	–
48.38	1.58564	–0.00069	0.00105	0.00050	–	0.00031
48.70	1.57585	–0.00007	0.00018	0.00064	–	–
48.71	1.57555	0.00024	0.00048	0.00094	–	–
51.02	1.50868	–0.00034	–0.00010	0.00023	–0.00061	0.00032
51.62	1.49232	0.00010	–	0.00042	–	–
53.40	1.44605	0.00013	–0.00105	–	–0.00031	–
55.04	1.40619	0.00013	0.00005	–	–0.00007	0.00086
55.44	1.39684	–0.00012	–	0.00032	–	–
57.09	1.35972	–0.00001	–	–	–	–
58.65	1.32664	0.00012	–	0.00021	–	–
58.84	1.32274	–0.00006	–	–0.00010	0.00020	0.00003
59.68	1.30580	–0.00017	0.00002	0.00044	0.00060	0.00049

those of Jäger et al. (1998) for various crystalline silicates, we find our 20 μm spectra at each temperature are best described by Mg-rich crystalline forsterite, again supporting the SXRD analysis. The 20 μm band dependence on temperature rather than time can be understood by noting that t_{short} is comparable to the ~5 hour time scale for the onset of the structural stall.

The initial absence of fine structure in both the 10 and 20 μm bands is a characteristic of non-crystalline materials (Tielens and Allamandola 1990). Although there is no long-range structural order in our initial sample, we have shown that there are well-defined SiO_n structural units. The Mg:Si ratio determines the average bulk-value for the number, N_{NBO},

of unshared, or non-bridging, O atoms per tetrahedron (Thompson 1996), while the tetrahedral arrangement itself is affected by two factors. First, the Mg cations may not be evenly distributed, leading to local variations of N_{NBO} whereby some regions will be rich in SiO_4, some in SiO_3, and some in SiO_2, etc. Second, there is a wider range in the inter-tetrahedral bond angle. For $N_{NBO} = 4$, there will also be large variations in the relative orientations of tetrahedra. Local variation in N_{NBO} means that the bulk N_{NBO} assumes a distribution between 0 and 4, but peaks around the crystalline value (in crystals, the even cation dispersion results in a single bulk N_{NBO}). Non-bridging O atoms provide a flow mechanism
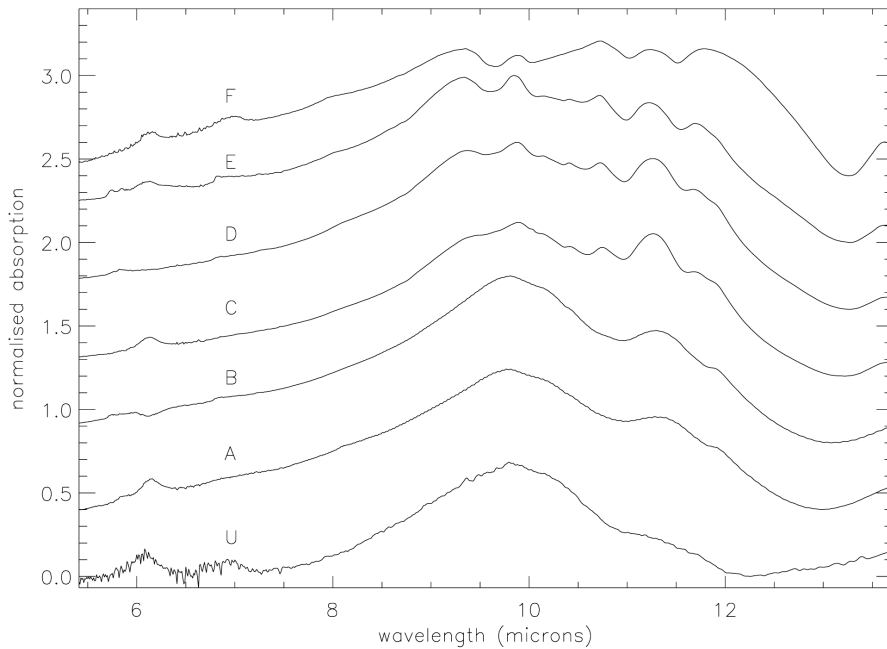
Fig. 7. IR 10 μm band spectra for annealed $MgSiO_3$ silicate samples collected for different temperatures and times: (U) unprocessed sample; (A) 873 K, t_{short}; (B) 873 K, t_{long}; (C) 970 K, t_{short}; (D) 970 K, t_{long}; (E) 1000 K, t_{short}; (F) 1000 K, t_{long}. For clarity, the spectra in this and in the following figure have been offset in the y-axis direction.
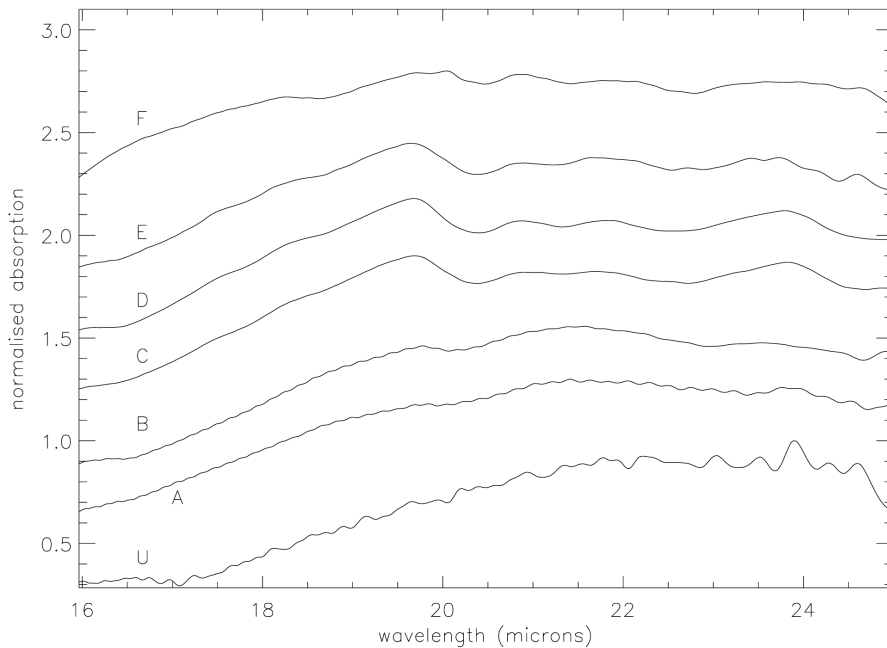

Fig. 8. IR 20 μm band spectra for annealed $MgSiO_3$ silicate samples, labeling is the same as in Fig. 7.

for the Mg cations (Thompson, Evans, and Jones 1996) so, regions initially rich in $N_{NBO} = 4$ are likely to be more susceptible to reordering since this is where conditions for the movement of both Mg and SiO_4 are most favorable. This is supported by the early formation of the 11.2 μm subfeature and forsterite SXRD features.

The frequency of the asymmetric Si-O stretch depends on whether the O is bridging or non-bridging. The lack of systematic variation of the amorphous 10 μm band peak intensity and shape relative to the 20 μm band is usually taken to mean that the 10 μm band components are insensitive to the longer-range inter-tetrahedral structure (McMillan 1984a, b). Given that the initially amorphous spectrum at 10 μm reflects the Si-O bond length dispersion, its evolution with time and

temperature suggests that during crystallization, the local SiO_n tetrahedral environment undergoes development throughout the annealing process. We also note the presence of certain features close to 9.3, 10.5, 10.8, and 11.8 μm which are usually attributed to enstatite rather than forsterite (Koike et al. 1981, 1993; Jäger et al. 1998). Observations of these features in Comet Hale-Bopp led Wooden et al. (1999) to propose crystalline pyroxene as a possible grain constituent. The absence of enstatite in our 1000 K SXRD data, however, questions the uniqueness of these features for making such identifications. Although arising from changes in the tetrahedral environment, the features may in fact not be reliant upon the adoption of a particular macroscopic crystalline structure. Alternatively, they could perhaps be due to ultra-dilute enstatite structures too weak/disordered to have been detected even in the summed SXRD data. However this last possibility would seem to contradict the assertion that crystalline pyroxene is less optically active than forsterite (Wooden et al. 1999), as our data would imply strong absorption in the 10 μm band but weak absorption in the 20 μm band. The possibility also remains that the features are unrelated to the crystallization of either $MgSiO_3$ or Mg_2SiO_4. Various pure amorphous Si_mO_n show features at 9.2–9.3 μm, accompanied by other features at ~8.4 μm and 11.4 μm (Si_2O_3) or 12.5 μm (SiO_2) and would at least be consistent with our proposal (below) that in promoting the ordering of Mg and SiO_4, annealing also enriches the SiO_2 content of the remaining amorphous silicate component.

DISCUSSION

Evolution of Crystalline Mg_2SiO_4 from Amorphous $MgSiO_3$

Our results show the evolution of a forsterite structure from an amorphous $MgSiO_3$ silicate, evidenced by both SXRD and IRS. Both techniques show that full crystallization does not occur at 1000 K. Instead, forsterite appears to coexist with a remaining amorphous component. Crystalline forsterite consists of a regular arrangement of Mg atoms and "free" SiO_4 tetrahedra, and we have argued that these more readily participate in the formation of ordered structures than do inter-linked tetrahedra. However, the amorphous component itself may play a role in inhibiting the availability of tetrahedra for crystallite formation. Our sample is originally formed as a hydrated precipitate (e.g., $MgSiO_3.H_2O$) and will, therefore, be rich in OH (hydroxyl, Steel and Duley 1987). Cosmic silicates will also have significant OH content as they too form in H-rich environments. Within a silicate, H atoms exist in a variety of states such as OH, SiH (hydride) or as interstitial H_2 molecules. Experiments on SiO_2 (Shelby 1994) show that both OH and SiH are removed by annealing at or above 973 K and are completely removed after several hours according to:

$$(Si - OH) + (Si - H) \rightarrow (Si - O - Si) + H_2 \qquad (7)$$
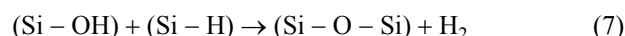
Other experiments confirm H_2 as the major component released (Morimoto et al. 1992). Below ~70% removal, the percentage removal curves for H_2 approximate those of simple diffusion but with an effective diffusion coefficient of 1.4×10^{-7} cm^2 s^{-1}, which is much lower than the value of 6×10^{-6} cm^2 s^{-1} expected for simple diffusion (Shelby 1997). Above 70% removal, the curves deviate significantly from simple diffusion. These results suggest the outflow of H_2 is controlled by the reaction rate of (7) (Morimoto et al. 1992). Furthermore, the activation energy of (7) lies between 260 and 266 kJ mol^{-1}, matching closely the 264 kJ mol^{-1} binding energy of the SiO-H bond (Shelby 1994). Thus, dehydrogenation is likely to be regulated by the breaking of the SiO-H bond. If we now assume that forming crystalline Mg_2SiO_4 in our sample involves all available Mg atoms, the removal of Mg, Si, and O in the ratio of 2:1:4 from a 1:1:3 composition will leave a residual component with a mass balanced Si:O ratio of 1:2, i.e., SiO_2. In other words, annealing an amorphous pyroxene composition rich in Si-OH and Si-H is likely to improve the Si-O-Si polymerization by recombining bonds freed up by dehydrogenation. It seems likely, therefore, that annealing not only promotes the initial formation of forsterite structures among regions rich in SiO_4, but at the same time, strengthens the remaining $SiO_{n<4}$ connectivity towards that of SiO_2. This component can then resist further structural reorganization due to the increased number of inter-tetrahedral bonds that would need to be broken (i.e., structural evolution stalls). An annealing-induced, solid-state phase separation between crystalline forsterite and a SiO_2-rich amorphous component would be consistent with both the SXRD and IRS results. Although it is well known in mineralogy that the incongruent melting of $MgSiO_3$ at liquidus temperature results in the formation of crystalline forsterite and a SiO_2 melt, the appearance of our samples post-annealing showed no signs of having melted. Indeed, the crystallization temperatures we report are even lower than those reported for silicates produced by other methods. The 11.2 μm olivine shoulder in the spectrum of our unprocessed silicate only appears in smoke produced silicates after substantial annealing at 1000 K (Hallenbeck, Nuth, and Daukantas 1998). This would seem consistent with our earlier assertion that gel desiccation does not produce silicates characteristic of freshly nucleated circumstellar materials, but rather ones where the transformation from chaotic assemblages to silicate has already occurred. Based on the results we have obtained, analysis of any crystalline forsterite grains returned by the Stardust mission later this decade should also reveal an associated amorphous silica component.

Reaction (7), as a polymerization mechanism, may also be the physical basis behind the stall phenonena reported by other authors. Hallenbeck, Nuth, and Daukantas (1998) suggested that their spectral stall might be related to changes in polymerization. In support of this, X-ray absorption spectroscopy at the Si K shell absorption edge for similar

samples (Thompson et al. 1996) showed the position of the absorption edge shifting in energy as a function of temperature. This effect is known to be characteristic of changes in the oxidation state of the absorbing species. Shifts were greatest at sub-crystallization temperatures, suggesting most alteration to the local Si environment occurred early in the annealing process. However, we note that the proposed dehydrogenation mechanism has yet to be verified experimentally for astrophysical silicates, and polymerization could proceed by some other means as well.

SiH and Cometary Silicates

Besides being verifiable in the laboratory, dehydrogenation may be observationally testable. It has been argued that, under certain conditions, the condensation of grains containing Si will result in the formation of SiH functional groups, giving absorption bands at 4.6 μm (Nuth and Moore 1988; Moore, Tanabe, and Nuth 1991). Such bands are seen in the IR source W33A and in lines of sight toward other proto-stellar embedded sources (Tegler et al. 1995). Often referred to as XCN features, they have also been attributed to solid CO and CN bonds (Lacey et al. 1984), CH_3NC (Larson et al. 1985), and OCN-ions trapped in grain surface ice mantles (Schutte and Greenberg 1997). More recent results, however, suggest a silicate origin. Laser evaporated silicate particles recondensed in H-rich atmospheres show a 4.6 μm feature (Blanco, Fonti, and Orofino 1999). The SiH carrier was confirmed by particles condensed in O-rich atmospheres failing to show the feature. In fact, the band position appears sensitive to the chemical environment of the Si atom and shifts from 4.39 μm in oxidised silicates to 4.74 μm in reduced solids (Nuth et al. 1992). Since cosmic grains will have condensed in H-rich atmospheres, it is likely that SiH and OH will be present in newly formed grains as directly incorporated defects. In the laboratory, molecular hydrogen reacts with silicates to form OH or OH/SiH pairs and can also exist as lone interstitial H2 molecules (Shelby 1994). Ionization, or direct displacement, can disrupt network bonds, whereupon void space hydrogen also forms SiOH and SiH. In crystalline olivines, incorporated protons associate with single O atoms to form tetrahedrally associated OH, isolated interstitial defects, or several OH molecules can group together at a cation vacancy site to charge balance the missing cation (Khisina et al. 2001, Braithwaite et al. 2002). Although nominally anhydrous, IR studies of both synthetic and naturally occurring terrestrial forsterite suggest cation vacancy defects occur as hydrous Mg-deficient olivine inclusions (i.e., $Mg_{2-x}v_xSiO_4H_{2x}$, where v_x denotes cation vacancy). Hydrogen also exists in naturally occurring terrestrial olivines as interstitial water, but in very low concentrations (<0.04 wt%, Khisina et al. 2001).

Ion implantation into Si at energies between 70 and 400 keV has also produced features between 4.5 and 5.5 μm

attributed to SiH (Moore, Tanabe, and Nuth 1991). Annealing at ~575 K for 20 min destroyed many of these features, but the band at 4.36 μm required a temperature of 975 K before it was destroyed. The stability of the SiH bands has also been shown to be affected by various chemical agents (Moore, Tanabe, and Nuth 1991). Consequently, Blanco, Fonti, and Orofino (1999) argued that SiH features are more likely to be seen either in new comets or where the cometary material has not been highly processed. If Reaction (7) occurs in annealed grains prior to incorporation, it is likely that only those comets without crystalline silicate features will exhibit the SiH band, suggesting Edgeworth-Kuiper belt rather than Oort cloud objects as the most likely candidates. However, if comet formation was ongoing throughout the history of the early solar nebula, old Oort cloud comets may also show the feature. For comets observed prior to the development of their comae, their low temperatures mean that the 5 μm region is dominated by reflected sunlight so that SiH should appear in absorption. For comets with SiH in small grains, the features should appear in emission at perihelion distances of 1.5–3 AU. At shorter distances, the emission features are likely to be swamped by continuum emission from small coma grains (Chyba, Sagan, and Mumma 1989).

If Reaction (7) is the route to increased polymerization, its efficacy will be determined by the relative abundance of SiOH and SiH, which is likely to be dependent on the method of manufacture for laboratory silicates or formation conditions and post-formation history for cosmic silicates (e.g., if ion implantation is a source of SiH in processed grains). However, detection of SiH is difficult both observationally and in the laboratory since it is easily masked by a strong atmospheric CO_2 absorption band (the ratio of the 10 μm silicate band peak intensity to the 4.6 μm band is ~30, Blanco, Fonti, and Orofino 1999). In future experiments, we will be paying attention to the 4.6 μm features present in our samples to shed more light on the dehydrogenation hypothesis.

Implications for Reconstructing the Thermal Histories of Grains

Although recognizing our sample as an idealized cosmic analogue, we have no reason to suppose its annealing history is unique to our method of manufacture. Indeed, the only prerequisite may be that the Mg cations are not evenly dispersed. This in itself is a likely feature of most amorphous silicates (Gurman 1990) and will almost certainly be so for cosmic grains, since condensation occurs in conditions far removed from thermodynamic equilibrium. Our results could, therefore, constitute the basis for a plausible explanation as to why crystalline pyroxene appears absent from comet spectra when it is a common component in its amorphous form. Annealed Mg-rich pyroxene may be spectroscopically indistinguishable at 20 μm from grains of "true" forsterite. In

the 10 μm band, the 9.3 μm and associated features may not be indicative of physical state as their carrier has not been definitively identified. Given the structural stall in the crystallite evolution, such features may, however, be indicators of thermal history. Thus, the formation of true crystalline enstatite grains by the annealing of amorphous pyroxenes may be harder to realize than their composition would suggest. The results reported here may, therefore, have implications for the reconstruction of grain histories as they indicate additional physical effects that need to be accounted for by theoretical models.

Conclusions and Future Work

We have presented the results of laboratory investigations into the crystallization of amorphous $MgSiO_3$ using SXRD and IRS. Annealing in the region of ~1000 K promotes the formation of crystalline forsterite structures with no substantial crystalline enstatite structures forming. This probably arises from the ordering of regions rich in proto-forsteritic units and is likely accompanied by an SiO_2 enrichment of the amorphous phase. The underlying mechanism may be an increase in the Si-O polymerization, and we have considered a potential dehydrogenation mechanism that could account for this. The proposed mechanism also has implications for astronomical observations of comets, and some of these have been addressed.

Several interesting points that will form the basis for further work have arisen. First, there is the question of how tied the present results are to the properties of the amorphous starting material. Related to this is the significance, if any, of any grain size effect on the progress of crystallization. There is also the question of the ambiguous 10 μm band features, and we aim to investigate how tightly these are tied to composition, crystal formation, or the amorphous phase. Finally, there is the question of the proposed dehydrogenation process and its role as a regulator of structural evolution. We plan to address these points as well as further refine our experimental technique. However, it is already clear that the use of complementary techniques offers greater scope for understanding the annealing process than could otherwise be achieved if each was used in isolation. Measurements designed to reproduce the astronomical data alone are unlikely to be sufficient in revealing the full picture behind grain histories as the parameter space explored by them is insufficient to allow unique solutions or constraints to be found.

Editorial Handling—Dr. Donald Brownlee

REFERENCES

Bailey M. E. 1987. The formation of comets in wind-driven shells around protostars. *Icarus* 69:70–82.

Bailey M. E. 1994. Formation of the outer solar system bodies: Comets and planetesimals. In *Asteroids, comets, meteors 1993: Proceedings of the 160th International Astronomical Union*, edited by Milani A., Di Martino M., and Cellino A. Dordrecht: Kluwer Academic Publishers. p. 443.

Bell K. R., Cassen P. M., Klahr H. H., and Henning T. 1997. The structure and appearance of protostellar accretion disks: Limits on disk flaring. *Astrophysical Journal* 486:372–387.

Blanco A., Bussoletti E., Colangeli L., Fonti S., Orofino V., and Stephens J. R. 1991. Laboratory spectra of amorphous and cristalline olivine: an application to comet Halley IR spectrum. In *Origin and evolution of interplanetary dust*, edited by Levasseur-Regourd A. C. and Hasegawa H. Dordrecht: Kluwer Academic Publishers. p. 125

Blanco A., Fonti S., and Orofino V. 1999. The 4.6 micron feature of SiH groups in silicate dust grains and infrared cometary spectra. *Planetary and Space Science* 47:781–785.

Bockelee-Morvan D., Gautier D., Hersant F., Hure J. M., and Robert F. 2002. Turbulent radial mixing in the solar nebula as the source of crystalline silicates in comets. *Astronomy & Astrophysics* 384: 1107–1118.

Borghesi A., Bussoletti E., and Colangeli L. 1995. Amorphous carbon grains: Laboratory measurements in the 2000 Å–40 μm range. *Astronomy & Astrophysics* 142:225–231.

Bradley J. P. 1994a. Chemically anomalous pre-accretionary irradiated grains in interplanetary dust from comets. *Science* 265: 925–928.

Bradley J. P. 1994b. Chemically anomalous pre-accreationary irradiated grains in interplanetary dust—Interstellar grains? *Meteoritics* 29:447.

Bradley J. P., Brownlee D. E., and Snow T. P. 1997. GEMS and other pre-accretionary irradiated grains in interplanetary dust particles. In *From stardust to planetesimals*, edited by Pendleton Y. J. and Tielens A. G. G. M. San Francisco: BookCrafters. p. 217.

Bradley J. P., Humecki H. J., and Germani M. S. 1992. Combined infrared and analytical electron microscope studies of interplanetary dust particles. *Astrophysical Journal* 294:643–651.

Bradley J. P., Snow T. P., Brownlee D. E., Keller L. P., Flynn G. J., and Miller M. 1998. Optical, mineralogical, and trace element properties of GEMS: Evaluating the interstellar connection. Proceedings, 29th Lunar and Planetary Science Conference p. 1737.

Bradley J. P., Snow T. P., Brownlee D. E., and Hanner M. S. 1999. Mg-rich olivine and pyroxene grains in primative meteoritic materials: Comparison with crystalline silicate data from ISO. In *Solid interstellar matter: The ISO revolution*, edited by d'Hendecourt L., Joblin C., and Jones A. Les Ullis: EDP Sciences. pp. 297–315.

Braithwaite J. S., Susko P. V., Wright K., and Catlow C. R. A. 2002. Hydrogen defects in forsterite: A test of the embedded cluster method. *Journal of Chemical Physics* 116:2628–2636.

Bregman J. D., Witteborn F. C., Allamandola L. J., Campins H., Wooden D. H., Rank D. M., Cohen M., and Tielens A. G. G. M. 1987. Airborne and ground-based spectrophotometry of Comet P/Halley from 5–13 micrometers. *Astronomy and Astrophysics* 187:616–620.

Brownlee D. E. 1990. Interstellar grains in the solar system. In *Interstellar processes*, edited by Hollenbach D. J. and Thronson H. A. Dordrecht: D. Reidel Publishing Company. pp 513–530.

Brucato J. R., Colangeli L., Mennella V., Palumbo P., and Bussoletti

E. 1999. Silicates in Hale-Bopp: Hints from laboratory studies. *Planetary and Space Science* 47:773–779.

Bussoletti E., Colangeli L., Borghesi A., and Orofino V. 1987. Tabulated extinction efficiencies for various types of submicron amorphous carbon grains in the wavelength range 1000 Å–300 μm. *Astronomy & Astrophysics Supplement Series* 70:257–268.

Campins H. and Ryan E. V. 1989. The identification of crystalline olivine in cometary silicates. *Astrophysical Journal* 341:1059–1066.

Chick K. M. and Cassen P. 1997. Thermal processing of interstellar dust grains in the primitive solar environment. *Astrophysical Journal* 477:398–409.

Chyba C. F., Sagan C., and Mumma M. J. 1989. The heliocentric evolution of cometary infrared spectra: Results from an organic grain model. *Icarus* 79:362–381.

Colangeli L., Mennella V., di Marino C., Rotundi A., and Bussoletti E. 1995. Simulation of the cometary 10 μm band by means of laboratory results on silicatic grains. *Astronomy & Astrophysics* 293:927–934.

Colangeli L., Mennella V., Rotundi A., Palumbo P., and Bussoletti E. 1996. Simulation of the cometary 10 μm band by laboratory data II. Extension to spectra available for different comets. *Astronomy & Astrophysics* 312:643–648.

Collins S. P., Cernik R. J., Pattison P., Bell A. M. T., and Fitch A. N. 1992. A 2-circle powder diffractometer for synchrotron radiation on station 2.3 at the srs. *Review of Scientific Instruments* 63:1013–1014.

Crovisier J., Brooke T. Y., Hanner M. S., Keller H. U., Lamy P. L., Altieri B., Bockerlee-Morvan D., Jorda L., Leech K., and Lellouch E. 1996. The infrared spectrum of Comet C/1995 O1 (Hale-Bopp) at 4.6 AU from the Sun. *Astronomy & Astrophysics* 315:L385–L388.

Crovisier J., Leech K., Bockerlee-Morvan D., Brooke T. Y., Hanner M. S., Altieri B., Keller H. U., and Lellouch E. 1997. The spectrum of comet Hale-Bopp (C/1995 O1) observed with the Infrared Space Observatory at 2.9 AU from the Sun. *Science* 275:1904–1907.

Day K. L. 1974. A possible identification of the 10-micron "silicate" feature. *Astrophysical Journal* 192:L15–L17.

Day K. L. 1976a. Further measurements of amorphous iron silicates. *Astrophysical Journal* 210:614–617.

Day K. L. 1976b. Synthetic phyllosilicates and the matrix material of C1 and C2 chondrites. *Icarus* 27:561–568.

Day K. L. 1977. Irradiation of magnesium silicates with MeV protons. *Monthly Notices of the Royal Astronomical Society* 178:49P–51P.

Delsemme A. H. 1999. The deuterium enrichment observed in recent comets is consistent with the cometary origin of seawater. *Planetary and Space Science* 47:125–131.

Demyk K., Jones A. P., Dartois E., Cox P., and d'Hendecourt L. 1999. The chemical composition of the silicate dust around RAFGL7009S and IRAS 19110+1045. *Astronomy & Astrophysics* 349:267–275.

Demyk K., Dartois E., Wiesemeyer H., Jones A. P., and d'Hendecourt L. 2000. Structure and chemical composition of the silicate dust around OH/IR stars. *Astronomy & Astrophysics* 364:170–178.

Demyk K., Carrez P., Leroux H., Cordier P., Jones, A. P., Borg J., Quirico E., Raynal P. I., and d'Hendecourt L. 2001. Structural and chemical alteration of crystalline olivine under low energy He$^+$ irradiation. *Astronomy & Astrophysics* 368:L38–L41.

Desch S. J. and Connolly H. C. 2002. A model of the thermal processing of particles in solar nebular shocks: Application to the cooling of chondrules. *Meteoritics & Planetary Science* 37:183–207.

Donn B. 1976. Comets, interstellar clouds, and star clusters in the study of comets: Part 2, Proceedings, 25th IAU Colloqium. *NASA Special Publication 393.* pp. 663–672.

Fernandez J. A. and Ip W. H. 1981. Dynamical evolution of a cometary swarm in the outer planetary region. *Icarus* 47:470–479.

Fernandez J. A. and Ip W. H. 1983. On the time evolution of the cometary influx in the region of the terrestrial planets. *Icarus* 54:377–387.

Greenberg J. M., Li A., Yamamoto T., and Kozasa T. 1996. On the crystalline silicate component of comet dust. *ASP Conference Proceedings Series* 104:497–506.

Grossman L. 1972. Condensation in the primitive solar nebula. *Geochimica et Cosmochimica Acta* 38:47–64.

Gurman S. J. 1990. Bond ordering in silicate glasses—A critique and a resolution. *Journal of Non-Crystalline Solids* 125:151–160.

Hallenbeck S. L., Nuth J. A., and Daukantas P. L. 1998. Mid-infrared spectral evolution of amorphous magnesium silicate smokes annealed in vacuum: Comparison to cometary spectra. *Icarus* 131:198–209.

Hallenbeck S. L., Nuth J. A., and Nelson R. N. 2000. Evolving optical properties of annealing silicate grains: From amorphous condensate to crystalline mineral. *Astrophysical Journal* 535:247–255.

Hanner M. S., Hackwell J. A., Russell R. W., and Lynch D. K. 1994a. Silicate emission feature in the spectrum of Comet Mueller 1993a. *Icarus* 112:490–495.

Hanner M. S., Lynch D. K., and Russell R. W. 1994b. The 8–13 micron spectra of comets and the composition of silicate grains. *Astrophysical Journal* 425:274–285.

Harker D. E. and Desch S. J. 2002. Annealing of silicate dust by nebular shocks at 10 AU. *Astrophysical Journal* 565:L109–L112.

Hart M. and Parrish W. 1986. Parallel beam powder diffractometry using synchrotron radiation. *Materials Science Forum* 9:39–46.

Hills J. G. 1982. The formation of comets by radiation pressure in the outer protosun. *Astronomical Journal* 87:906–910.

Hills J. G. and Sandford M. T. 1983. The formation of comets by radiation pressure in the outer protosun. II—Dependence on the radiation-grain coupling. III—Dependence on the anisotropy of the radiation field. *Astronomical Journal* 88:1519–1530.

Hukins D. W. L. 1981. *X-ray diffraction by disordered and ordered systems*. Oxford: Pergamon Press. p. 87.

Hwang J. S. and Tien C. 1996. XRAYSCAN: An indexing program considering dense spurious peaks in an optimisation method. *Chinese Journal of Physics* 34:47–57.

Ip W. H. and Fernandez J. A. 1988. Exchange of condensed matter among the outer and terrestrial protoplanets and the effect on surface impact and atmospheric accretion. *Icarus* 74:47–61.

Jäger C., Mutschke H., Begemann B., Dorschner J., and Henning T. 1994. Steps towards interstellar silicate mineralogy 1. Laboratory results of a silicate glass of mean cosmic composition. *Astronomy & Astrophysics* 292:641–655.

Jäger C., Molster F. J., Dorschner J., Henning T., Mutschke H., and Waters L. B. F. M. 1998. Steps towards interstellar silicate mineralogy IV. The crystalline revolution. *Astronomy & Astrophysics* 339:904–916.

Jessberger E. K., Christoforidis A., and Kissel J. 1988. Aspects of the major element composition of Halley's dust. *Nature* 332:691–695.

Joswiak D. J., Brownlee D. E., Bradley J. P., and Schlutter D. J. 1996. Systematic analysis of major element distributions in GEMS from high speed IDPs. Proceedings, 27th Lunar and Planetary Science Conference. pp. 625–626.

Kemper F., Waters L. B. F. M., de Koter A., and Tielens A. G. G. M. 2001. Crystallinity versus mass-loss rate in asymptotic giant branch stars. *Astronomy & Astrophysics* 369:132–141.

Khisina N. R., Wirth R., Andrut M., and Ukhanov A. V. 2001. Extrinsic and intrinsic mode of hydrogen occurrence in natural olivines: FTIR and TEM investigation. *Physics and Chemisty of Minerals* 28:291–301.

Koike C., Hasegawa H., Asada N., and Hattori T. 1981. The extinction coefficients in mid- and far-infrared of silicate and iron oxide minerals of interest for astronomical observations. *Astrophysics and Space Science* 79:77–85.

Koike C., Shibai H., and Tuchiyama A. 1993. Extinction of olivine and pyroxene in the mid- and far-infrared. *Monthly Notices of the Royal Astronomical Society* 264:654–658.

Kratschmer W. and Huffman D. R. 1979. Infrared extinction of heavy ion irradiated and amorphous olivine, with applications to interstellar dust. *Astrophysics and Space Science* 61:195–203.

Lacey J. H., Baas F., Allamandola L. J., Persson S. E., McGregor P. J., Londsdale C. J., Geballe T. R., and Van de Bult C. E. P. 1984. 4.6 micron absorption features due to solid CO and cyano group molecules toward compact infrared sources. *Astrophysical Journal* 276:533–543.

Larson H. P., Davies D. S., Black H. H., and Fink U. 1985. Interstellar absorption features toward the compact infrared source W33A. *Astrophysical Journal* 299:873–880.

Lawler M. E., Brownlee D. E., Temple S., and Wheelock M. M. 1989. Iron, magnesium, and silicon in dust from comet Halley. *Icarus* 80:225–242.

Lutz D., Feuchtgruber H., Genzel R., Kunze D., Rigopoulou D., Spoon H. W. W., Wright C. M., Egami E., Katterloher R., Sturm E., Wieprecht E., Sternberg A., Moorwood A. F. M., and de Graauw T. 1996. SWS observations of the galactic center. *Astronomy & Astrophysics* 315:L269–L272.

Malfait K., Waelkens C., Waters L. B. F. M., Vandenbussche B., Huygen E., and de Graauw M. S. 1998. The spectrum of the young star HD 100546 observed with the Infrared Space Observatory. *Astronomy & Astrophysics* 332:L25–L28.

Messenger S. and Walker R. M. 1996. Possible association of isotopically anomalous cluster IDPs with comet Schwassmann-Wachmann 3. Proceedings, 27th Lunar and Planetary Science Conference. pp. 1906–1907.

Messenger S. and Walker R. M. 1997. Evidence for molecular cloud material in meteorites and interplanetary dust. In *Astrophysical implications of the laboratory studies of presolar materials*, edited by Bernatowicz T. J. and Zinner E. Woodbury: American Institute of Physics. pp. 545–564.

Messenger S., Clemett S. J., Keller L. P., Thomas K. L., Chillier X. D. F., and Zare R. N. 1995. Chemical and mineralogical studies of an extremely D-rich IDP. *Meteoritics* 30:546–547.

Messenger S., Walker R. M., Clemett S. J., and Zare R. N. 1996. Deuterium enrichments in cluster IDPs. Proceedings, 27th Lunar and Planetary Science Conference. pp. 867–868.

Messenger S., Keller L. P., and Thomas-Keprta K. L. 1997. Complementary transmission electron microscopy and hydrogen isotopic measurements of interplanetary dust. *Meteoritics & Planetary Science* 32:A9.

McMillan P. 1984a. Structural studies of silicate glasses and melts—Applications and limitations of Raman spectroscopy. *American Mineralogist* 69:622–644.

McMillan P. 1984b. A Raman spectroscopic study of glasses in the system CaO-MgO-SiO$_2$. *American Mineralogist* 69:645–659.

Moore M. H., Tanabe T., and Nuth J. A. 1991. The -SiH vibrational stretch as an indicator of the chemical state of the interstellar grains. *Astrophysical Journal* 373:L31–L34.

Morimoto Y., Igarashi T., Sugahara H., and Nasu S. 1992. Analysis of gas-release from vitreous silica. *Journal of Non-Crystalline Solids* 139:35–46.

Munro I. H. 1997. Synchrotron radiation research in the UK. *Journal of Synchrotron Radiation* 4:344–358.

Napier W. M. and Clube S. V. M. 1997. Our cometary environment. *Reports on Progress in Physics* 60:293–343.

Ney E. P. 1982. Optical and infrared observations of bright comets in the range 0.5 micrometers to 20 micrometers. In *Comets*, edited by Wilkening L. L. Tucson: University of Arizona Press. pp. 323–340.

Nuth J. A. 1999. Constraints on nebular dynamics based on observations of annealed magnesium silicate grains in comets and disks around Herbig Ae and Be stars. Proceedings, 30th Lunar and Planetary Science Conference. pp. 1726–1727.

Nuth J. A. and Hecht J. A. 1990. Signatures of ageing silicate dust. *Astrophysics and Space Science* 163:79–94.

Nuth J. A. and Moore M. H. 1988. -SiH and the unidentified 4.6 micron feature. *Astronomy & Astrophysics* 187:513–518.

Nuth J. A., Moore M. H., Tanabe T., and Kraus G. 1992. The -SiH vibrational stretch as an indicator of the oxidation state of silicon in a cometary or asteroidal regolith. *Icarus* 98:207–210.

Nuth J. A., Hill H. G. M., and Kletetschka G. 2000. Determining the ages of comets from the fraction of crystalline dust. *Nature* 406: 275–276.

Oort J. H. 1950. The structure of the cloud of comets surrounding the solar system and a hypothesis concerning its origin. *Bulletin of the Astronomical Institutes of the Netherlands* 11:91–110.

Petaev M. I. and Wood J. A. 1996. Condensation in the solar nebula: Effects of partial isolation of condensates from the residual gases. Proceedings, 27th Lunar and Planetary Science Conference. pp. 1023–1024.

Prinn R. G. 1990. On neglect of nonlinear momentum terms in solar nebula accretion disk models. *Astrophysical Journal* 348:725–729.

Rietmeijer F. J. M., Nuth J. A., and Karner J. M. 1999. Metastable eutectic condensation in a Mg-Fe-SiO-H$_2$-O$_2$ Vapour: Analogues to circumstellar dust. *Astrophysical Journal* 527:395–404.

Rietmeijer F. J. M., Hallenbeck S. L., Nuth J. A., and Karner J. M. 2002. Amorphous magnesiosilicate smokes annealed in vacuum: The evolution of magnesium silicates in circumstellar and cometary dust. *Icarus* 156:269–286.

Sabatier G. 1950. La cristallisation, par chauffage, des gels mixtes de silice et de magnésie. *Comptes Rendues de l'Académie des Sciences* 230:1962–1964.

Safronov V. S. 1972. Ejection of bodies from the solar system in the course of the accumulation of the giant planets and the formation of a cometary cloud. In *The motion, evolution, and origin of comets*, edited by Chebotarev G. A. et al. New York: Springer Verlag. pp. 329–334.

Schultze H., Kissel J., and Jessberger E. K. 1997. Chemistry and mineralogy of Comet Halley's dust. In *From stardust to planetesimals*, edited by Pendleton Y. J. and Tielens A. G. G. M. San Francisco: BookCrafters. pp. 397–414.

Schutte W. A. and Greenberg J. M. 1997. Further evidence for the OCN assignment to the XCN band in astrophysical ice analogues. *Astronomy & Astrophysics* 317:L43–L46.

Shelby J. E. 1994. Protonic species in vitreous silica. *Journal of Non-Crystalline Solids* 179:138–147.

Sitko M., Grady C. A., Russell R. W., Lynch D. K., Hanner M. S., Perez M. R., Bjorkman K. S., and Dewinter W. 2000. Infalling planetesimals in pre-main stellar systems. In *Protostars and planets IV*, edited by Mannings V., Boss A. P., and Russell S. S. Tucson: University of Arizona Press. p. 613.

Sogawa H. and Kozasa T. 1999. On the origin of crystalline silicate in circumstellar envelopes of oxygen-rich asymptotic giant branch stars. *Astrophysical Journal* 516:L33–L36.

Steel T. M. and Duley W. W. 1987. A 217.5 nanometer absorption feature in the spectrum of small silicate particles. *Astrophyscial*

Journal 315:337–339.

Stevenson D. J. 1990. Chemical heterogeneity and imperfect mixing in the solar nebula. *Astrophysical Journal* 348:730–737.

Tang C. C., Bushnell-Wye G., and Cernik R. J. 1998. New high- and low-temperature apparatus for synchrotron polycrystalline X-ray diffraction. *Journal of Synchrotron Radiation* 5:929–931.

Tegler S. C., Weinstraub D. A., Rettig T. W., Pendleton Y. J., Whittet D. C. B., and Kulesa C. A. 1995. Evidence for chemical processing of precometary ice grains in circumstellar environments of pre-main sequence stars. *Astrophysical Journal* 439:279–287.

Thompson S. P. 1996. 10 μm silicate bands and the structure of grains. *Astrophysical Letters & Communications* 33:299–303.

Thompson S. P. and Tang C. C. 2001. Laboratory investigation of crystallisation in annealed amorphous MgSiO$_3$. *Astronomy & Astrophysics* 368:721–729.

Thompson S. P., Evans A., and Jones A. 1996. Structural evolution in thermally processed silicates. *Astronomy & Astrophysics* 308:309–320.

Tielens A. G. G. M. and Allamandola L. J. 1990. Composition, structure, and chemistry of interstellar dust. In *Interstellar processes*, edited by Hollenbach D. J. and Thronson H. A. Dordrecht: Reidel Publishing Company. pp. 297–469.

Tielens A. G. G. M., Waters L. B. F. M., Molster F. J., and Justtanont K. 1998. Circumstellar silicate mineralogy. *Astrophysics and Space Science* 255:415–426.

Waassmaier D. and Kiferl A. 1995. New analytical scattering factors for free atoms and ions. *Acta Crystallographica* A51:416–423.

Waelkens C., Waters L. B. F. M., de Graauw M. S., Huygen E., Malfait K., Plets H., Vandenbussche B., Beintema D. A., Boxhoorn D. R., Habing H. J., Heras A. M., Kester D. J. M., Lahuis F., Morris P. W., Roelfsema P. R., Salama A., Siebenmorgen R., Trams N. R., van der Blick N. S., Valentijn E. A., and Wasselius P. R. 1996. SWS observations of young main sequence stars with dusty circumstellar disks. *Astronomy & Astrophysics* 315:L245–L248.

Weissman P. R. 1995. The Kuiper belt. *Annual Review of Astronomy and Astrophysics* 33:327–358.

Whittaker E. J. W. 1981. *Crystallography.* Oxford: Pergamon Press. p. 232.

Wooden D. H., Harker D. E., Woodward C. E., Butner H. M., Koike C., Witteborn F. C., and McMurty C. W. 1999. Silicate mineralogy of the dust in the inner coma of Comet C/1995 O1 (Hale-Bopp) pre- and post-perihelion. *Astrophysical Journal* 517:1034–1058.

Wooden D. H., Butner H. M., Harker D. E., and Woodward C. E. 2000. Mg-rich silicate crystals in Comet Hale-Bopp: ISM relics or solar nebular condensates? *Icarus* 143:126–137.